

Influence of Equatorial Waves on the Genesis of Super Typhoon Haiyan (2013)

SHOUJUAN SHU

Key Laboratory of Mesoscale Severe Weather, Ministry of Education, and School of Atmospheric Science, Nanjing University, Nanjing, China, and Department of Meteorology, The Pennsylvania State University, University Park, Pennsylvania

FUQING ZHANG

Department of Meteorology, The Pennsylvania State University, University Park, Pennsylvania

(Manuscript received 12 January 2015, in final form 11 August 2015)

ABSTRACT

The influence of equatorial wave disturbances on the genesis of Super Typhoon Haiyan (2013) is investigated through spectral, composite, and ensemble sensitivity analysis of various observational datasets in combination with predictions from an operational ensemble. Under the favorable large-scale environmental conditions of the Asian monsoon combined with the Madden–Julian oscillation (MJO), the incipient Haiyan develops from a cyclonic disturbance that originates from a train of westward-propagating mixed Rossby–gravity (MRG) waves. Haiyan eventually develops in the monsoon trough region at the leading edge of the moist MJO phase that has strong low-level convergence, high moisture content, and weak shear, along with high sea surface temperature. These favorable environmental conditions promote the intensification of deep moist convection that facilitates the development of the cyclonic disturbance from an MRG wave into a tropical depression, which later intensifies rapidly into Super Typhoon Haiyan, one of the world’s strongest and most destructive tropical storms ever recorded. Results from ensemble sensitivity analyses are consistent with this finding and further show that the uncertainties in tropical waves and their interactions can impact the large-scale environment surrounding Haiyan’s precursor and therefore limit the predictability of tropical cyclone formation and intensity. The better-performing members tend to have a stronger initial MRG wave disturbance, which provides a stronger initial seed for the later development of the storm, as well as a stronger moist MJO wave in the tropical region, which not only promotes deep convection near the precursor location, but also reduces the environmental vertical wind shear by strengthening the tropical westerlies.

1. Introduction

Each year approximately 80–90 tropical cyclones (TCs) form globally (Frank and Young 2007), about one-third of which, on average, develop in the western North Pacific (WNP), the most active basin for TC genesis. Tropical cyclogenesis (TCG) has been regarded as one of the least understood phenomena in tropical meteorology. This is partly due to the lack of in situ observations capturing TC formation over the remote open ocean and partly due to the complex multiscale interactions ranging from large-scale environment to small-scale moist convection. Moreover, there are even

greater challenges for TCG in the WNP, which has larger complexity and variability in the background environment compared to other TC basins. For example, the Pacific monsoon trough and the associated southwesterlies are important components of the large-scale circulation during the typhoon seasons unique in the WNP (Fu et al. 2012).

A list of large-scale conditions favorable for TCG is given in Tory and Frank (2010), which complemented the first global TC genesis climatology of Gray (1968): sea surface temperature (SST) above 26.5°C coupled with a relatively deep oceanic mixed layer of 50 m, a deep surface-based layer of conditional instability with organized deep convection in an area with mean large-scale ascent and high midlevel humidity, enhanced low-level cyclonic vorticity, and weak to moderate vertical wind shear. Recently, Nolan and McGauley (2014) further show that easterly wind shear is statistically more

Corresponding author address: Professor Fuqing Zhang, Department of Meteorology, The Pennsylvania State University, 503 Walker Building, University Park, PA 16802.
E-mail: fzhang@psu.edu

favorable for TC genesis than westerly shear. Many studies have also shown that TC formation in the WNP is also closely related to the large-scale flow patterns, which evolve with the seasons from a winter trade environment to a summer monsoon. The winter trade easterlies are dominant over the WNP from January to April and transform to a monsoonal pattern with cross-equatorial westerlies converging with the easterlies from May to August. The trough pattern remains largely unchanged but with a somewhat southward shift because of the retreat of the Asian monsoon during the transition period of September–December (e.g., [Ritchie and Holland 1999](#)). The monsoonal trough region, which extends from the Indochina Peninsula in the west to the east of the Philippine Sea, provides a favorable environment for the formation of multiday persistent cloud clusters that frequently grow into TCs in the WNP ([Gray 1968, 1998](#)). The attendant cyclonic shear of the horizontal wind, as well as the confluence zone along the monsoon trough, provides enhanced dynamical conditions for TC development. A recent study of [Yoshida and Ishikawa \(2013\)](#) revealed that the patterns associated with the monsoon trough account for about 64% of the total TCGs in the WNP, consistent with previous studies ([Frank 1982](#); [Briegel and Frank 1997](#); [Ritchie and Holland 1999](#)). Apart from its direct dynamical influence on TCG, [Holland \(1995\)](#) and [Sobel and Bretherton \(1999\)](#) argued that the monsoonal confluence region can trap tropical waves in the mid-to-lower troposphere through wave energy accumulation ([Chang and Webster 1990](#)), which organizes the enhanced tropical convection into mesoscale convective systems and increases the potential for cyclogenesis. [Ritchie and Holland \(1999\)](#) further pointed out that once the confluence region is established, the low-level external influence provided by other processes is likely to induce further convection and cyclogenesis.

TCs are sometimes organized in the southeast quadrant of the monsoon gyre that is an organized low-level cyclonic vortex associated with a nearly circular depression ~2500 km in width, often persisting for several weeks over the WNP ([Lander 1994](#); [Chen et al. 1996](#)). An observational study by [Wu et al. \(2013\)](#) showed that WNP TCs often formed near the center of the monsoon gyre and the northeast end of the enhanced southwesterly flows under the influence of an upper-level anticyclone and a relatively weak vertical wind shear. A follow-up idealized numerical study by [Liang et al. \(2014\)](#) further suggested that the Rossby wave energy dispersion of the monsoon gyre can also play an important role in the TC formation through enhancing southwesterly flow on the east-southeast periphery of the monsoon gyre.

Besides the abovementioned favorable environment for precursors to evolve into TCs in the WNP, it is commonly observed that TCG is also closely related to equatorial waves from synoptic to intraseasonal scales that include mixed Rossby–gravity (MRG) waves, tropical depression (TD)-type waves, equatorial Rossby waves, Kelvin waves, and the Madden–Julian oscillation (MJO) (e.g., [Frank and Roundy 2006](#)). The MJOs, which have characteristics of eastward propagation along the equator at the intraseasonal time scale, are found to have a strong influence on the TC activities in several basins. More specifically, the MJO westerly phase could modulate environmental fields by producing low-level cyclonic horizontal shear ([Frank and Roundy 2006](#)) and increasing midlevel moisture ([Camargo et al. 2009](#)), which may lead to significantly more TCs in the active phase than in the inactive phase of MJO ([Liebmann et al. 1994](#)). The MJO could also promote higher-frequency waves to amplify through scale contraction and energy accumulation by establishing a convective envelope that is favorable for TCG ([Nakazawa 1986](#)). For example, [Maloney and Dickinson \(2003\)](#) found that the perturbation kinetic energy corresponding to a TD-type disturbance is significantly higher during the active phase of MJOs.

Equatorial Rossby (ER) waves also carry substantial variance in the boreal summer and fall ([Roundy and Frank 2004](#)) and are important for modulating TC formations in the WNP. [Frank and Roundy \(2006\)](#) found that the coherent annual cycle in the ER wave activity coincides well with the TC season. [Molinari et al. \(2007\)](#) documented several cases of WNP TCG that are related to enhanced background convection and low-level cyclonic vorticity associated with the ER waves.

The MRG waves are synoptic, equatorially trapped waves with wavelengths of 6000–10 000 km, where the convection lags the low pressure center by about a quarter wavelength ([Matsuno 1966](#); [Takayabu and Nitta 1993](#); [Dunkerton and Baldwin 1995](#)). TD-type disturbances are off-equatorial wave perturbations characterized by deep convection occurring in the vicinity of the cyclone center with shorter wavelengths (2000–4000 km). Despite differences in structure and preferred region, the MRG waves and TD-type disturbances are sometimes dynamically connected. Studies (e.g., [Dickinson and Molinari 2002](#); [Takayabu and Nitta 1993](#)) showed that lower-tropospheric MRG waves first moved away from the equator and were gradually transformed into an off-equatorial TD-type disturbance, which eventually developed into a mature TC under the convective MJO environment. [Aiyer and Molinari \(2003\)](#) further confirmed the contribution of the tropical asymmetric MJO to the transition and rapid growing of

the MRG perturbations in an idealized numerical model. Fu et al. (2007) analyzed TCG events in the WNP during 2000–01 and found that 40% of the TD-type wave trains originated from the MRG waves. The upper-tropospheric MRG waves over the far eastern Pacific may sometimes provide “seeds” for TCG over the WNP as shown in Zhou and Wang (2007). However, the detailed evolution from an equatorially trapped wave to an off-equatorial TD and the associated mechanism are not well understood.

Rossby wave energy dispersion from a preexisting TC is also recently found to be capable of initiating TCG in the WNP. While a TC moves northwestward as a result of mean steering flow and the planetary vorticity gradient, Rossby waves emit energy southeastward (Anthes 1982; Luo 1994; McDonald 1998). As a result, a synoptic-scale wave train with alternating anticyclonic and cyclonic perturbations forms in its wake (Carr and Elsberry 1994, 1995). The TC induced energy dispersion (TCED) and its relation to TCG has been demonstrated using satellite observations and model simulations (Li et al. 2003; Li and Fu 2006; Fu et al. 2007). Chen and Tam (2012) found that the southeastward-propagating TCED can give rise to the equatorial atmospheric response with a temporal scale and structure consistent with the equatorially trapped MRG waves. Besides direct seeds from these northwestward-propagating disturbances, the waves’ gyre also provides a favorable environment to protect the protovortex to strengthen into an incipient tropical cyclone (Wang et al. 2012).

Easterly wave troughs within the trade wind system may sometimes directly develop into TCs in the equatorial Pacific (Heta 1990, 1991; Chen et al. 2008). They can also enhance existing genesis potentials through scale contraction and energy accumulation in the monsoon trough region (Ritchie and Holland 1999; Kuo et al. 2001).

In summary, a great deal of research has revealed that TCGs over the WNP can be mainly attributed to large-scale environmental flow patterns associated with the monsoon trough and equatorial waves with a wide range of scales. Statistical studies showed that TCs often appear to be generated in conditions with multiple flow patterns (Yoshida and Ishikawa 2013) and that TCGs related to multiple waves are roughly twice as many as those related to a single wave (Chen and Chou 2014; Schreck and Molinari 2011), suggesting the important roles of multiprocesses or multiscale interactions in TCG. Most of the previous studies focused on the relationship between multiple waves or large-scale flow patterns and TCGs from a climatological perspective. It remains largely unresolved how those aforementioned precursors interact with equatorial waves in promoting TCG.

One recent storm that highlights the current problems in forecasting TC genesis and intensity change is Super Typhoon Haiyan, which formed from an area of low pressure on 2 November 2013 and evolved rapidly to typhoon intensity 3 days later with subsequent landfall in the Philippines at nearly peak intensity (Lander et al. 2014). The present study seeks to understand the influence of tropical disturbances on the genesis of Haiyan through spectral, composite, and ensemble sensitivity analysis of various observational datasets in combination with forecasts from the operational ensemble prediction system (EPS) of the European Center for Medium-Range Forecasting (ECMWF).

Section 2 introduces the data and analysis methods. The synoptic overview and genesis environment for Haiyan (2013) are presented in section 3. The wave features related to the precursor and its ensemble predictability for Haiyan are examined in section 4 and 5, respectively. Section 6 further contrasts the fundamental differences between developers and nondevelopers among different ensemble members with an emphasis on interactions between multiple tropical waves. Conclusions are given in section 7.

2. Data and methodology

a. Data

The 6-hourly $1^\circ \times 1^\circ$ global gridded dataset from the National Centers for Environmental Prediction (NCEP) final analysis (FNL) is used to analyze the storm-related vorticity maxima before and during the genesis of Haiyan, as well as the associated large-scale environment. The Japan Meteorological Agency (JMA) postseason best-track estimate of position and intensity is used to track the storm right after TCG of Haiyan, when the storm was first classified as a tropical depression at 0600 UTC 3 November. The position of the disturbance before TCG is defined by the circulation center with the maximum 850-hPa relative vorticity (from the FNL analysis).

For a proxy of deep convection, both the 3-hourly Tropical Rainfall Measuring Mission (TRMM) Multi-satellite Precipitation Analysis (TRMM 3B42; Huffman et al. 2007) with a $0.25^\circ \times 0.25^\circ$ spatial resolution and the daily outgoing longwave radiation (OLR) data from the National Oceanic and Atmospheric Administration (NOAA) satellite on a 2.5° latitude–longitude grid (Liebmann and Smith 1996) are employed. The Reynolds weekly mean SST reanalysis (Reynolds et al. 2002) with a horizontal resolution of $1^\circ \times 1^\circ$ provided by NOAA Cooperative Institute for Research in Environmental Science (CIRES) Climate Diagnostics Center (CDC) are used herein, which can be obtained online at <http://www.cdc.noaa.gov>.

The predictability of the genesis of Haiyan is evaluated using the 51-member ensemble (including one control forecast and 50 perturbations) provided by the operational EPS system of the ECMWF. The ECMWF ensemble perturbations are constructed using singular vectors that capture the fastest-growing errors in the first 48 h (Buizza and Palmer 1995) along with stochastic perturbations accounting for uncertainties in parameterized physical processes. The 15-day EPS 0000 UTC forecasts for the period 27 October–11 November 2013, which covered the entire life cycle of Haiyan, are obtained through The Observing System Research and Predictability Experiment (THORPEX) Integrated Grand Global Ensemble (TIGGE; Bougeault et al. 2010) project with a horizontal resolution of $0.25^\circ \times 0.25^\circ$ and eight mandatory pressure levels (1000, 925, 850, 700, 500, 300, 250, and 200 hPa, except for the geopotential height).

b. Analysis methods

The space–time wave decomposition of Wheeler and Kiladis (1999) is used to extract tropical wave signals by filtering the wave period and truncating the wavenumber according to characteristics of wave propagation. A positive (negative) wavenumber denotes eastward (westward) propagation. Three dominant types of equatorial waves, MJOs, MRGs, and TD-type disturbances, are considered in this work, which are extracted as follows: a wavenumber ranging from 0 to 5 and a period ranging from 20 to 90 days for MJOs, a wavenumber from -3.96 to -13.2 (with wavelengths of 3000–10 000 km) and a period from 3 to 6 days for MRG waves, and a wavenumber from -9.9 to -39.6 (with wavelengths of 1000–4000 km) and a period from 3 to 6 days for TD-type disturbances (Liebmann and Hendon 1990; Takayabu and Nitta 1993; Dunkerton and Baldwin 1995; Chang et al. 1996). All of these features will be referred to as equatorial waves because they reside in equatorial regions and share wavelike properties.

To assess the environmental and storm-related factors that affect the genesis of Haiyan, an ensemble-based sensitivity analysis based on ensemble correlations is performed following previous studies (e.g., Zhang 2005; Hawblitzel et al. 2007; Torn and Hakim 2008; Sippel and Zhang 2008, 2010; Munsell et al. 2013). Both direct correlations and partial correlations will be used to examine the influence of environmental factors and tropical waves on the genesis of Haiyan. In the framework of statistical significance with a sample size of 51, a correlation of 0.35, 0.27, and 0.23 is statistically different from 0 with over 99%, 95%, and 90% confidence, respectively. Although it is well understood that correlation does not imply causality, it can be used to demonstrate that ensemble behavior is consistent with physical reasoning developed in previous studies.

3. Synoptic overview and genesis environment

Haiyan was the thirtieth named storm of the 2013 Pacific typhoon season. It was first tracked as an area of low pressure several hundred kilometers east-southeast of Pohnpei in the Federated States of Micronesia on 2 November 2013. The system developed into a tropical depression the following day. After becoming a tropical storm at 0000 UTC 4 November, the system began a period of rapid intensification that brought it to typhoon intensity by 1800 UTC 5 November when it tracked generally westward along the southern periphery of a subtropical ridge. According to the estimate of the Joint Typhoon Warning Center, the system was assessed as a category-5-equivalent super typhoon on the Saffir–Simpson hurricane wind scale by 6 November and attained its peak intensity with 1-min sustained winds of 315 km h^{-1} (195 mph) at 1800 UTC 7 November, becoming the most powerful storm ever recorded to strike land (Lander et al. 2014). Several hours later, the eye of the cyclone made its first landfall in the Philippines at Guiuan, Eastern Samar, at peak intensity with 10-min sustained winds of 230 km h^{-1} (145 mph) as estimated by the Philippine Atmospheric, Geophysical and Astronomical Services Administration (PAGASA), and then five additional landfalls in the Philippines before emerging over the South China Sea.

Although whether or not it was the strongest storm in recorded history was in dispute (partly owing to the lack of a direct measure of intensity along with using different standards of reporting wind speeds of TCs by different agencies), Super Typhoon Haiyan caused catastrophic loss of lives and properties with its extremely strong winds, strong storm surge, and the associated landslides and flash floods, particularly in the Philippines, making it the deadliest Philippine typhoon on record, killing about 6300 people along with 1000 missing (NDRRMC 2014).

Figure 1 shows the observed large-scale low-level patterns at 0600 UTC 30 October, 96 h before genesis of Haiyan (referred to herein as -96 h). A confluent flow region between the monsoonal westerlies and equatorial trade easterlies, collocated with the maximum gradient of zonal flow and elongated cyclonic shear, forms over the region $4^\circ\text{--}12^\circ\text{N}$, $145^\circ\text{--}165^\circ\text{E}$. The storm gets closer and comes to the well-developed cyclonic monsoon trough area at -24 h , a region with high cyclonic vorticity and convergence that is favorable for the development of an initial vortex: it is an area conducive to sustained moist convection (Holland 1995) and for energy accumulation from various traveling waves (Chang and Webster 1990).

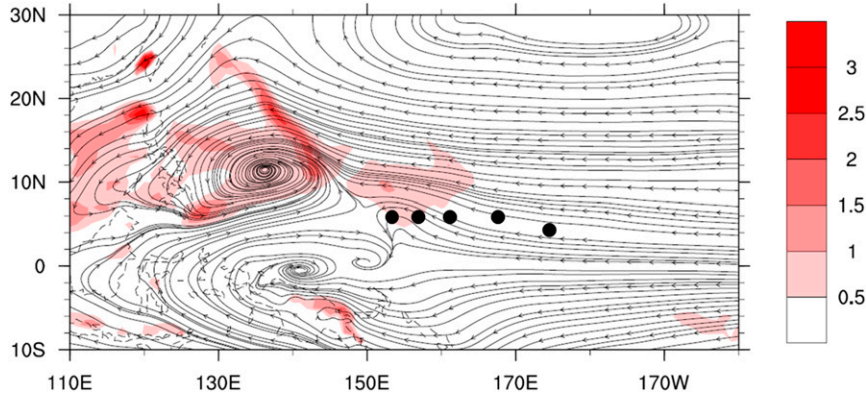


FIG. 1. The time-mean streamlines and relative vorticity at 850 hPa prior to TCG. The five black dots from east to west represent the centers of the precursor at time -96 h (0600 UTC 30 Oct), -72 h (0600 UTC 31 Oct), -48 h (0600 UTC 1 Nov), -24 h (0600 UTC 2 Nov), and 0 h (0600 UTC 3 Nov) prior to TCG. The shading indicates values of relative vorticity greater than $5 \times 10^{-6} \text{ s}^{-1}$.

The vertical wind shear (VWS) has long been recognized as a key detrimental factor affecting TC intensity. Earlier studies (Gray 1968; Merrill 1988) showed that the intensifying TCs tended to have weaker vertical shear than the nonintensifying ones. Modeling results indicated that a weak vertical wind shear could result in rapid intensification of a TC (e.g., Frank and Ritchie

1999, 2001; Tao and Zhang 2014). A recent observational study of Shu et al. (2012) found that the intensifying cases tend to develop in warmer water, lower vertical shear, and more easterly upper-tropospheric flow than do the nonintensifying cases over the WNP.

Figure 2a shows mean spatial distribution of the VWS by subtracting the 850- from 200-hPa wind vectors

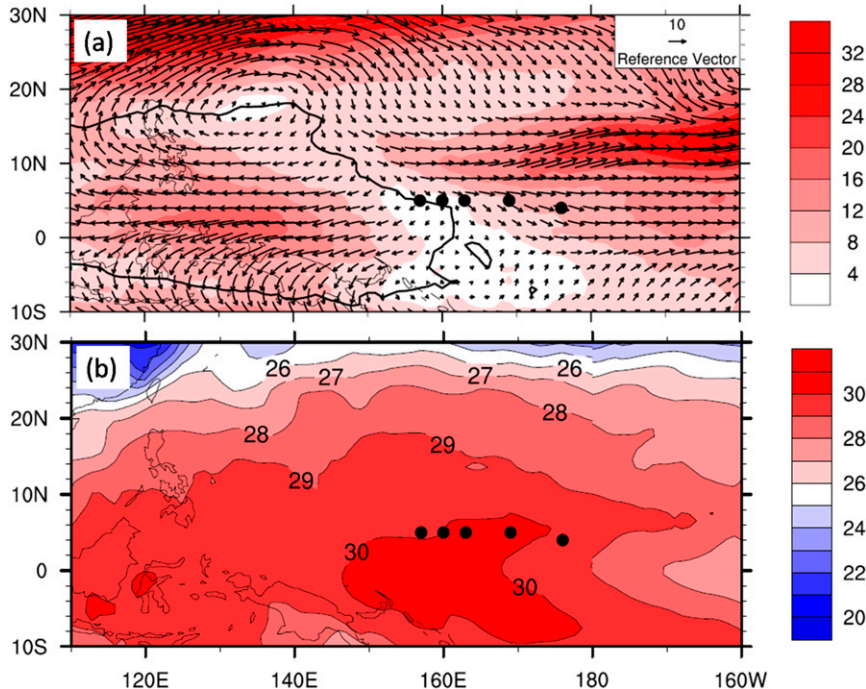


FIG. 2. The time-mean (a) 850–200-hPa VWS (vectors), amplitude of the VWS (shading; 4 m s^{-1} intervals starting at 0 m s^{-1}), and region of easterly shear (black thick contour) and (b) sea surface temperature (SST, $^{\circ}\text{C}$). The five black dots from east to west represent the centers of the precursor at time -96 , -72 , -48 , -24 , and 0 h prior to TCG.

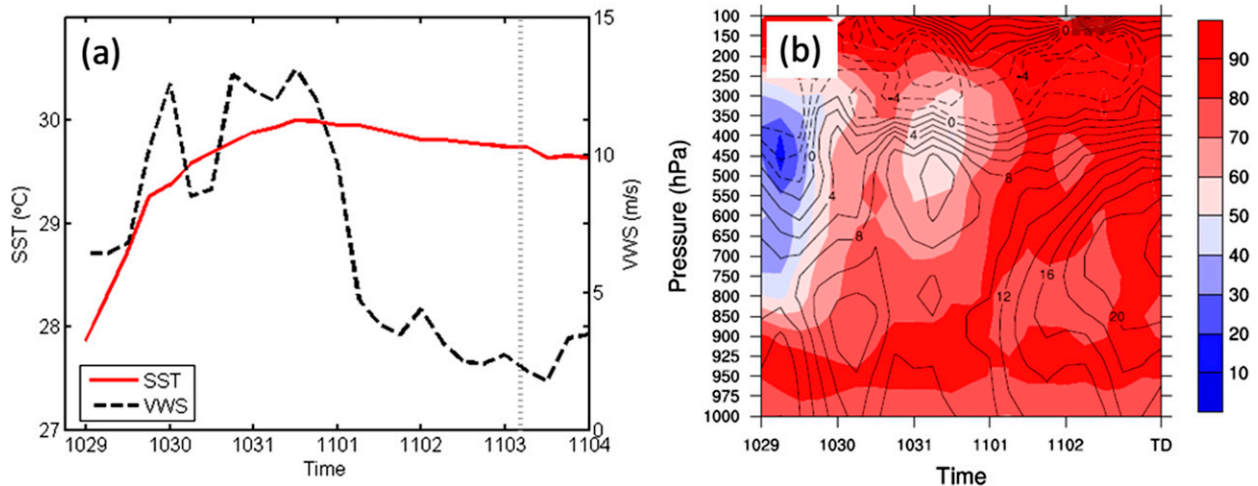


FIG. 3. Time variation of (a) SST (solid) and large-scale VWS (dashed) averaged over the $6^\circ \times 6^\circ$ and $10^\circ \times 10^\circ$ storm-relative domain, respectively, and (b) relative vorticity (contours every $0.2 \times 10^{-5} \text{ s}^{-1}$, negative values dashed) and relative humidity (shading, 10% intervals) averaged over the $10^\circ \times 10^\circ$ storm-relative domain. The dotted vertical line in (a) and letters “TD” in abscissa of (b) indicate the time of TCG.

before the formation of Haiyan averaged over a 7-day period (0600 UTC 27 October–0600 UTC 3 November). Strong easterly shear (within the scope of the black thick contour) lies along the western equator while westerly shear exists eastward and farther poleward. Along with the westward-moving storm during the preceding days, it approaches a region with generally weak and easterly shear, which not only favors the intensification of the disturbance but also provides an environment for wave accumulation. Past studies showed that the easterly wind shear is more likely (than the westerly shear) to trap wave energy in the lower troposphere and is therefore more favorable for cyclogenesis (Tuleya and Kurihara 1981; Webster and Chang 1998; Wang and Xie 1996; Shu et al. 2014). Beginning around -48 h (0600 UTC 1 November), the area-averaged large-scale shear decreases to no more than 5 m s^{-1} , which is conducive to synoptic-scale ascent before and during TCG (Bracken and Bosart 2000) (Fig. 3a). Figure 2b shows the map of mean SSTs averaged from 15 October through 13 November spanning over the genesis time. From -72 h (0600 UTC 31 October), the area-averaged SST underlying the disturbance is about 30°C —very favorable for TC development. In the meantime, there is a marked increase and deepening in the low-level moisture, accompanying evident strengthening of the relative vorticity at 0600 UTC 30 October and 0000 UTC 1 November (Fig. 3b).

From above analysis, the large-scale environment is very favorable for TC development with anomalously warm sea surface, abundant lower-to-midtropospheric moisture, and a rather weak vertical wind shear several days before TCG. We will demonstrate below that

Haiyan developed after a precursor tropical wave disturbance moved into such a favorable environment.

4. Synoptic overview on the origin of Haiyan’s precursor

Figure 4 shows the longitude–time Hovmöller diagrams of the unfiltered and filtered 850-hPa meridional wind V and OLR (only regions of active convection) near the equator during a period from 0000 UTC 27 October to 0000 UTC 7 November, which spans the genesis and early development stages of Haiyan. The filtered fields are obtained through the space–time wave decomposition method of Wheeler and Kiladis (1999), which include the 3–6-day MRG and TD-type waves as well as the MJO signal (Fig. 4b).

A large area of active deep convection originates west of 120°E before 0000 UTC 28 October that then propagates eastward and reaches about 155°E by 0000 UTC 1 November (Fig. 4a). This is apparently associated with the leading edge of an active phase of the MJO as can be seen from the MJO-filtered signal (Fig. 4b). The 3–6-day disturbances with a longer wavelength and a westward phase speed of approximately 16.4 m s^{-1} and an eastward group speed of roughly 6.5 m s^{-1} (Fig. 4b) are consistent with the westward phase speed (eastward group speed) of $15\text{--}20 \text{ m s}^{-1}$ (5 m s^{-1}) of the MRG waves identified in Pacific in previous studies (Liebmann and Hendon 1990; Takayabu and Nitta 1993; Dunkerton and Baldwin 1995). The MRG waves are also evidenced by the large equatorial meridional wind component in the unfiltered field (Fig. 4a), suggesting that the incipient

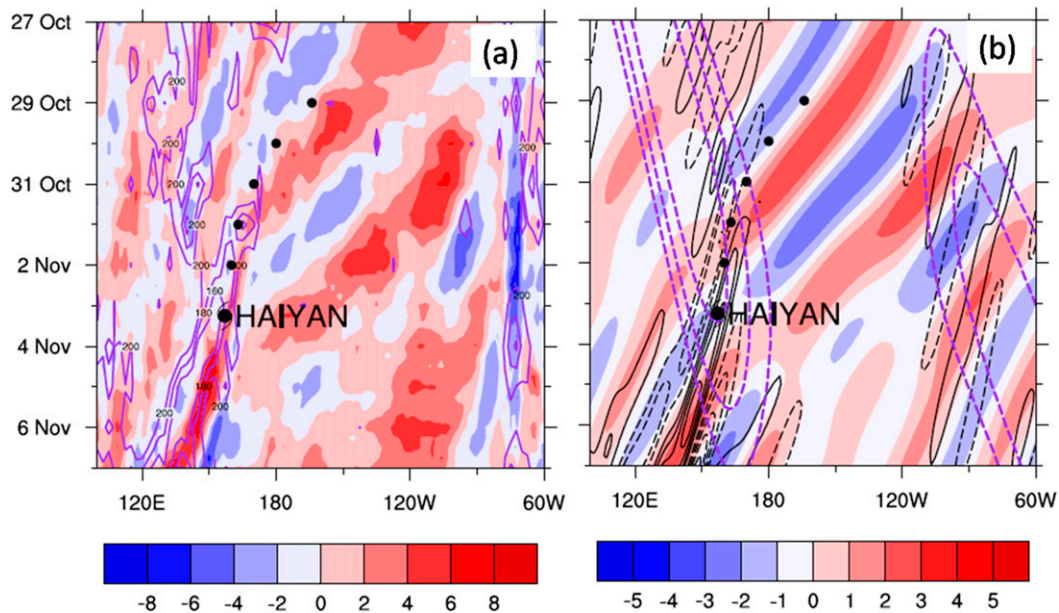


FIG. 4. Longitude–time plot of (a) unfiltered 850-hPa meridional wind averaged over 5°S – 5°N (shaded; 2 m s^{-1} intervals starting at 0 m s^{-1}) and unfiltered OLR at the equator (purple contoured; 20 W m^{-2} intervals below 200 W m^{-2}) and (b) 3–6-day, 3000–10 000-km filtered 850-hPa meridional wind averaged over 5°S – 5°N (shaded; 1 m s^{-1} intervals starting at 0 m s^{-1}) and 3–6-day, 1000–4000-km filtered 850-hPa meridional wind averaged over 0° – 10°N (black contoured; negative values dashed), and 20–90-day, >8000-km filtered OLR (purple dashed contours; 2 W m^{-2} intervals between -10 and -6 W m^{-2}). The typhoon symbol indicates the location of TCG for Haiyan, and the black dots mean the locations of Haiyan’s precursor before TCG.

Haiyan (indicated by the black dots at different times) originates from a cyclonic MRG disturbance.

Besides the westward-moving MRG waves and the eastward-moving convective activities associated with the MJO, there are also evident TD-type waves that may be related to the TCED from a preexisting typhoon (Krosa), which formed at 142°E on 27 October. Southeastward energy dispersion from a northwestward-moving TC has been previously suggested in the literature to be capable of initiating or enhancing new tropical cyclone development (e.g., Anthes 1982; Luo 1994; McDonald 1998; Ge et al. 2010). However, the eastward energy dispersion associated with the TCED from Krosa is only evident before 0000 UTC 31 October, whose influence on the development of Haiyan is likely limited.

The slowly varying background flow (Fig. 5) associated with the MJO, on the other hand, not only provides the large-scale low-level convergence, but also helps to moisten the lower-to-midlevel troposphere near the location of TCG. The precursor of Haiyan from the MRG wave packet rapidly intensifies on the TD scale after it propagates into the leading edge of the moist phase of the MJO on 1 November (Fig. 4).

Figure 6 shows the evolution of the 850-hPa 3–6-day bandpass-filtered winds and unfiltered 24-h-accumulated precipitation from TRMM. At 5 days prior to TCG, a

counterclockwise MRG circulation of interest appeared east of the date line (about 180° – 140°W , marked by an ellipse; Fig. 6a). The heavy rain region is located at the leading edge of the downstream cross-equatorial southerlies, about one-quarter wavelength ahead of the cyclonic center. The structure is consistent with those commonly observed MRG waves (e.g., Kiladis et al. 2009), although the unfiltered rainfall suggests this structure may be also associated with the low-frequency intertropical convergence zone (ITCZ).

The longitude–height cross sections of meridional wind anomaly and relative vorticity on the equator (Fig. 7) indicate a clear wave train of alternating southerlies and northerlies mainly in the upper troposphere with maximum amplitude of meridional wind at 400 hPa before 0000 UTC 29 October. The cyclonic MRG gyre located to the east of the date line tilts eastward with elevation whose vertical extent reaches the lower troposphere (Figs. 7c–f), in accordance with the previous observational study of Zhou and Wang (2007). One day later at 0600 UTC 30 October, the disturbance moves westward and contracts in spatial scale but still maintains the structure of an MRG wave (Fig. 7c) with convection ahead of the cyclonic center (Fig. 6b). During its continuous westward journey on the next day, the MRG disturbance turns to the northwest

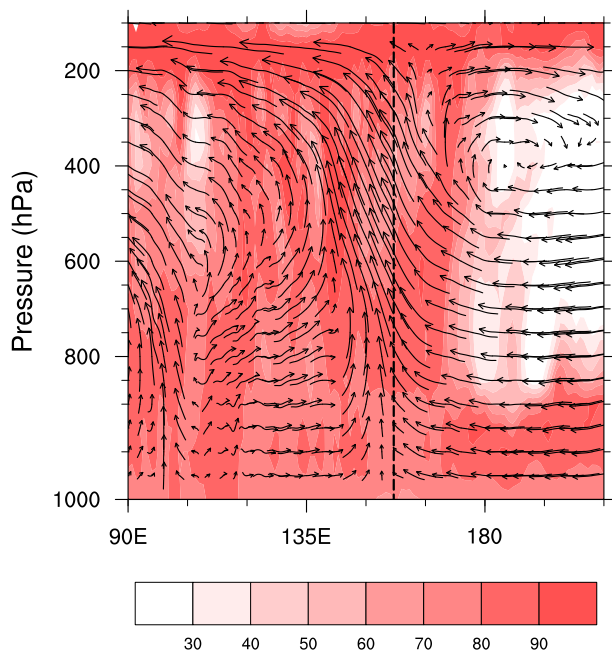


FIG. 5. The 7-day (0600 UTC 27 Oct–0600 UTC 3 Nov) mean U – W circulation and relative humidity (shaded every 10%) on MJO scale. The dashed line means the location of TCG.

and begins to attain some TD-type wave characteristics, with wavelength reducing considerably and deep convection developing around the cyclonic gyre, exhibiting hybrid properties of both MRG- and TD-type waves (Figs. 6c, 7d). By 0600 UTC 1 November, the cyclonic disturbance evolves into a TD-type disturbance with a nearly upright structure along with smaller-scale convection concentrating over the vortex center (Figs. 6d and 7e,f) as it moves northwestward to about 5°N and gradually evolves into the precursor of Haiyan. As mentioned earlier, the surrounding large-scale environment is favorable for the development of this TC precursor. The two processes (one from the east—the transition of the equatorial MRG waves to off-equatorial TD-type perturbations, and the other one from the west—the TCED from preexisting Typhoon Krosa) causes the formation of a clear wave train with well-defined cyclonic and anticyclonic circulations appearing in the tropical region (from about 115°E to 170°W) in Fig. 6. Transition from the MRG waves to TD-type disturbances was also found in earlier studies (e.g., Zhou and Wang 2007; Aiyyer and Molinari 2003).

5. Ensemble performance and predictability of Haiyan's genesis

The operational ECMWF ensemble archived in the TIGGE dataset is used here to understand the uncertainties

and underlying dynamics in the forecasting of Haiyan's genesis. The current study is complementary to a recent study of Qian et al. (2013), which used such a dataset to examine the uncertainties in the track forecasts of Super Typhoon Megi (2010), which also hit the Philippines, during and after its peak intensity stages.

Besides the control (CTRL) member in the ECMWF ensemble forecasts, the other 50 members of the ECMWF EPS are produced with perturbed initial conditions along with stochastic model physics, which provide a wide variety of intensity forecasts that highlights the uncertainties in predicting Haiyan's genesis. Figure 8 shows the time evolution of the storm intensities in terms of 850-hPa relative vorticity (Vor_{850}) from all ensemble members and FNL. As seen from the ensemble spread in terms of the standard deviation of the estimated intensity among the members, the uncertainty increases over longer forecast lead times. Although most members are weaker than the FNL estimated intensity (likely owing to the use of a higher effective analysis resolution by FNL), the genesis of Haiyan is forecasted by about one-third of the 50 members. Based on the area-averaged Vor_{850} verified against the FNL during the genesis period (0000 UTC 29 October–0000 UTC 4 November), we select two subgroups of ensemble members representing developers and nondevelopers to further identify dynamical processes that are key to the TCG: the GOOD and POOR groups consist of 10 members that have the smallest and largest mean intensity forecast errors, respectively. Figures 9f,g show a mosaic of the 10 selected GOOD members and the 10 selected POOR members depicting Vor_{850} at 0000 UTC 4 November (192h into the forecast). It can be seen that there are apparent uncertainties in this medium-range forecast for the genesis of Haiyan as evidenced by the large systematic divergence between the GOOD and POOR groups.

We first examine the performance of the CTRL member in the ECMWF ensemble for the forecast initialized at 0000 UTC 27 October in comparison with the FNL observational analysis. The top two rows in Fig. 10 show the time evolution of relative humidity (RH), relative vorticity, horizontal divergence, and high-level temperature anomalies in the vertical column averaged over the $10^{\circ} \times 10^{\circ}$ storm-relative domain for FNL (Figs. 10a–d) and CTRL (Figs. 10e–h). Despite being somewhat weaker in magnitude, the CTRL-forecasted Haiyan's precursor and immediate environment are overall consistent with those in the observational analysis. Figures 11a–d further show the comparison of the Hovmöller diagrams of the Wheeler–Kiladis filtered fields for both the CTRL forecast and the FNL analysis at different scales. The CTRL-forecasted wave

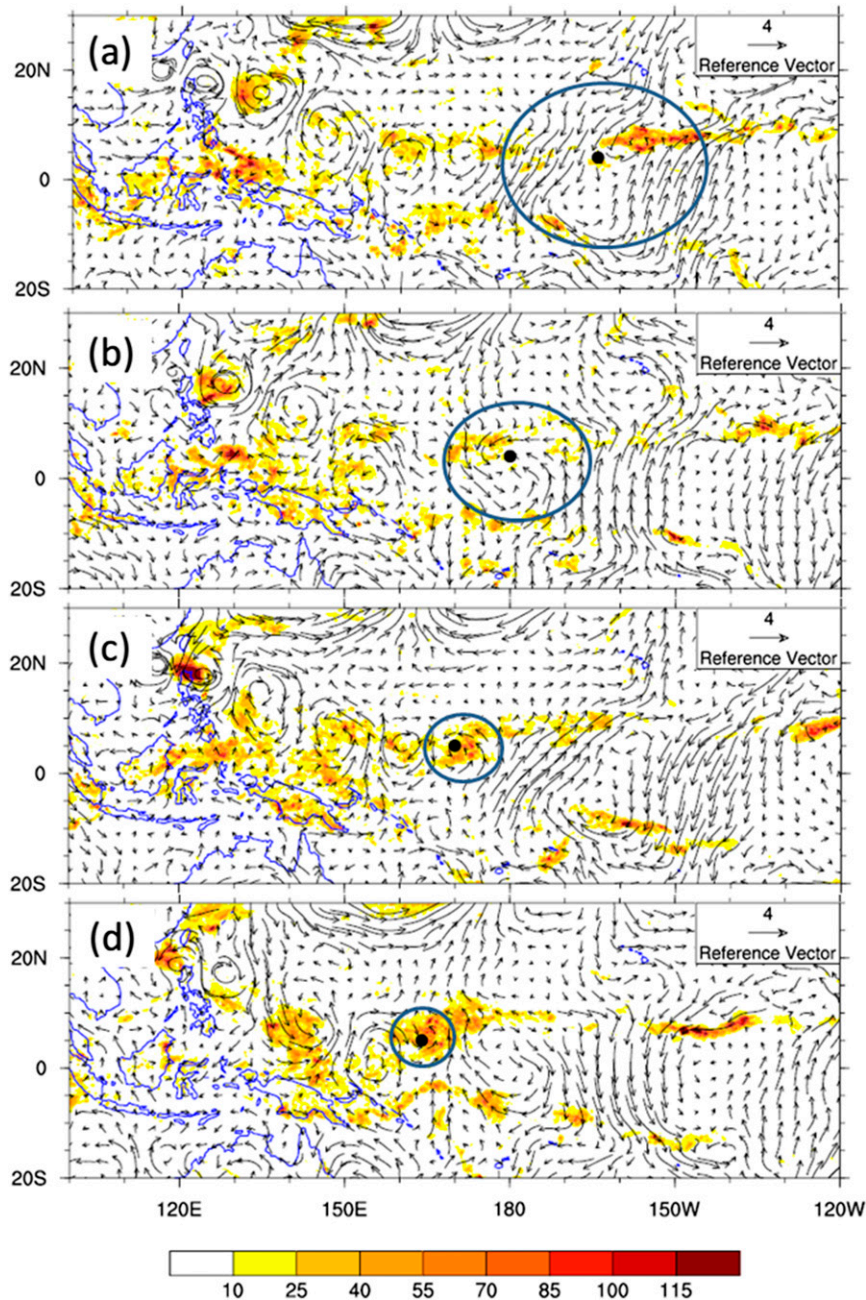


FIG. 6. The 3–6-day bandpass-filtered wind vectors at 850 hPa and unfiltered 24-h-accumulated TRMM precipitation (shading > 10 mm) at (a) -120 h (0600 UTC 29 Oct), (b) -96 h (0600 UTC 30 Oct), (c) -72 h (0600 UTC 31 Oct), and (d) -48 h (0600 UTC 1 Nov) prior to TCG. The ellipses indicate the cyclonic circulation associated with the initial vortex. The filled black circles mean the locations of the vortex center prior to TCG.

patterns of both the MRG precursor from the east, and the TD-type disturbances associated with the preexisting tropical cyclone (Krosa) from the west (Fig. 11c) exhibit similar patterns to that observed (Fig. 11a) before 0000 UTC 31 October. On the scale of the MJO, the zonal wind propagation to the location of the

precursor from CTRL (Fig. 11d) is also similar to that seen in the observation (Fig. 11b), except for a weaker intensity and a slightly slower movement speed than the FNL analysis. These comparisons suggest that the CTRL ensemble of ECMWF EPS captures the primary processes precedent to the genesis of Haiyan by

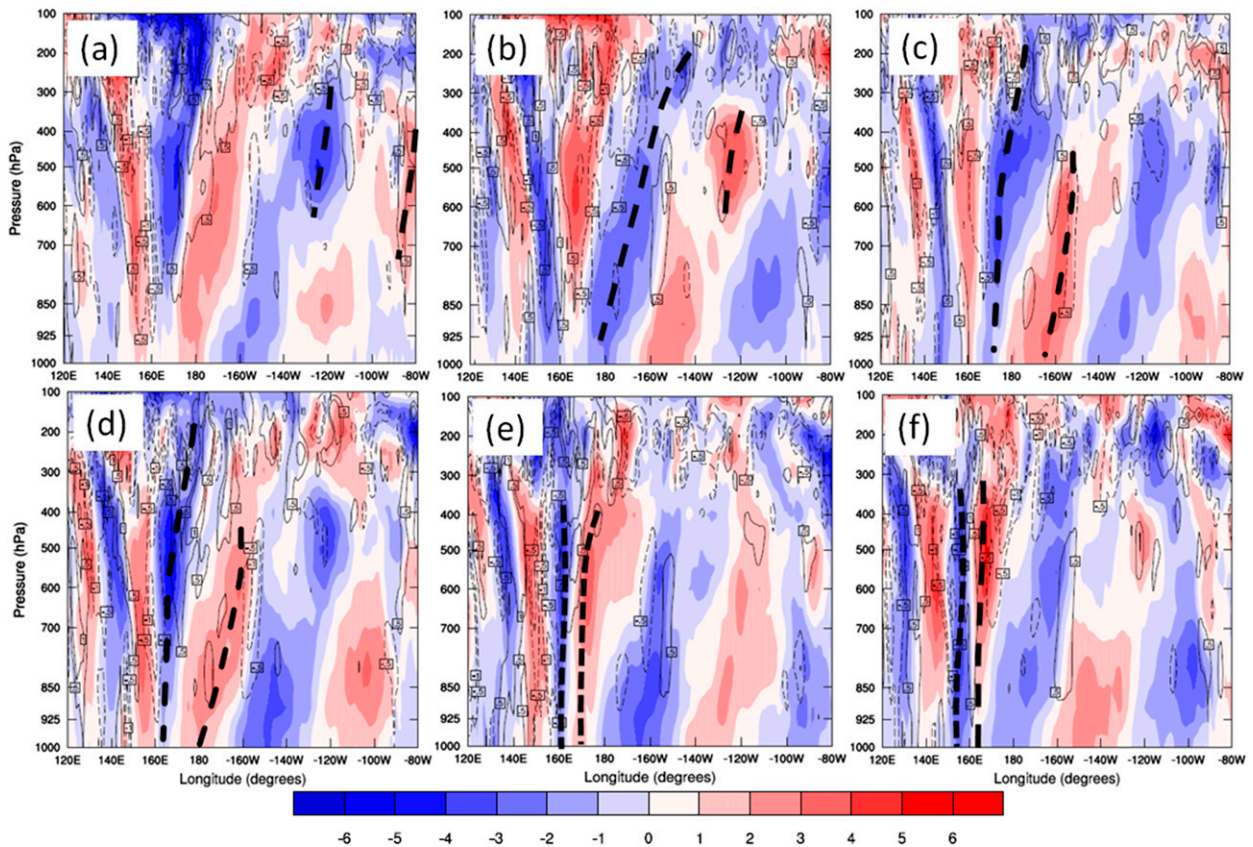


FIG. 7. Longitude–height section of meridional wind anomaly (shaded; 1 m s^{-1} intervals) and relative vorticity (contoured; $0.5 \times 10^{-5} \text{ s}^{-1}$ intervals without 0 s^{-1} for simplicity, negative values dashed) on the equator at (a) 0000 UTC 27 Oct, (b) 0000 UTC 29 Oct, (c) 0000 UTC 30 Oct, (d) 0000 UTC 31 Oct, (e) 0000 UTC 1 Nov, and (f) 0000 UTC 2 Nov. The two dashed lines indicate the vertical penetration and transition from an upper-level MRG gyre to a TD-type cyclonic disturbance.

predicting well the structure and evolution of the attendant equatorial waves. We will next further examine the predictability of the storm (and its precursor) before and during the genesis of Haiyan.

Within the GOOD group, member 29 (Figs. 10i–l) well predicts the intensity and structure of Haiyan’s precursor in 5–8-day lead times while the forecast by member 50 in the POOR group fails completely (Figs. 10m–p) in comparison to the CTRL (Figs. 10e–h) and observations (Figs. 10a–d). Before the forecast hour 60 (valid at 1200 UTC 29 October), there are little differences between members with the RH of 60% above 850 hPa (Figs. 10a,e,i,m). After 78 h into the integration (valid at 0600 UTC 30 October), differences between the members start to emerge, with lower-tropospheric RH increasing and deepening in member 29 and CTRL, consistent with the observation, but decreasing in member 50. The relative vorticity in the lower-to-midtroposphere also becomes stronger in member 29 than that in member 50 below 400 hPa (Figs. 10j,n); similar differences are also clear in the upper levels

(Figs. 10c,g,k,o). From the forecast hour 108 (valid at 1200 UTC 31 October), deep convection develops throughout the vertical column with increased RH dominating the entire troposphere in member 29 as observed in FNL (Figs. 10a,i), in contrast with a dry midtroposphere in member 50 (Fig. 10m). Meanwhile, significant upper-tropospheric (200–400 hPa) warming also appears in member 29 and CTRL (Figs. 10h,l), both of which compare favorably with that observed in FNL (Fig. 10d). Concurrent with the upper-level warming (Figs. 10d,h,l), the strong upper-level divergence (Figs. 10c,g,k) occurs at about the same time in FNL, CTRL, and member 29, indicating an occurrence of deep convection. From forecast hour 108 to TCG, along with the burst of deep moist convection, the lower-tropospheric vorticity and convergence, as well as the upper-level divergence of the precursor all enhance rapidly (Figs. 10b,c,f,g,j,k) in member 29 (as well as in CTRL and FNL). This finding is consistent with the recent study of Cecelski et al. (2014), who found that the 400–150-hPa layer-averaged warming could result in the

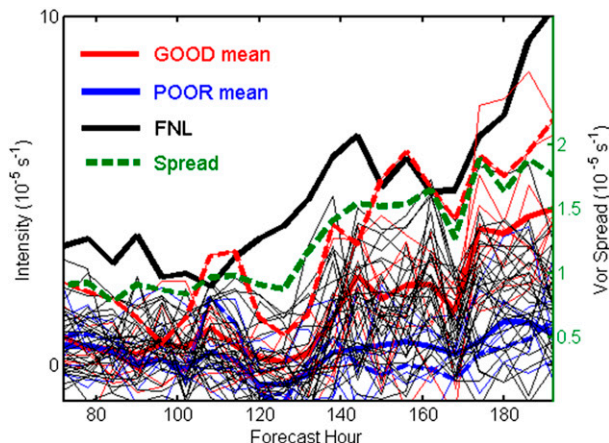


FIG. 8. Evolution of the averaged 850-hPa relative vorticity (10^{-5} s^{-1}) of all members (thin lines), GOOD mean (thick red line), POOR mean (thick blue line), member 29 (thick red dashed line), member 50 (thick blue dashed line), FNL observation (thick black line), and member spread (10^{-5} s^{-1} ; green dashed line). The thin red, blue, and black lines correspond to the 10 selected GOOD, POOR, and the remaining members, respectively.

decreasing of mean sea level pressure and, thus, favor the fast development of the storm. Member 50 does not exhibit similar characteristics as those fields seen in member 29 (Figs. 10m–p) and thus essentially fails to develop the precursor into Haiyan.

Figure 12 compares the large-scale environmental conditions between members 29 and 50 at selected times. At the beginning of the integration, little difference exists between these two ensemble members (not shown). By 0060 UTC 29 October (54 h into the forecast; Figs. 12a–c), clear differences start to emerge, with stronger equatorial southerly winds to the southeast and northerly winds to the southwest in member 29 but not in member 50 (marked by open arrows in Fig. 12c), suggesting a stronger cyclonic MRG wave disturbance for the former. After 108 h into the integration (valid at 0012 UTC 31 October; Figs. 12d–f), besides a much stronger cyclonic vorticity, member 29 depicts a considerably moister midlevel atmosphere practically to the western portion of the MRG vortex and weaker shear environment than that in member 50 (Fig. 12f). By the end of observed transition period (from MRG gyre to TD-type precursor; Figs. 12g–i), there exists drastic differences in lower-level vorticity and midlevel humidity, as well as vertical wind shear between these two members: the GOOD member (member 29) has a larger region of significant midlevel moisture that covers most parts of the TC environment as well as a larger area of weaker VWS that lies on the eastern motion path of the TC, making the environment more favorable for precursor development (Fig. 12i). Conversely, the nondeveloping vortex in the POOR

member (member 50) is accompanied by dry advection and stronger VWS on its motion path, creating an unfavorable environment for the TC precursor to develop. As a result, the precursor intensifies into a tropical depression in member 29 (Fig. 12j) but does not in member 50 (Fig. 12k) one day later.

The difference between these two members can also be clearly seen in the Hovmöller diagrams of the Wheeler–Kiladis wave-filtered variables shown in the bottom two panels of Fig. 11: magnitudes of both the MRG and TD-type waves are considerably stronger in member 29 than that in member 50 (Figs. 11e,g). As we stated earlier, member 50 with a significantly weaker MRG wave will have the weak cyclonic and anticyclonic TD-type disturbances. For the MJO signal, positive westerlies propagate to the location of incipient Haiyan in member 29 (Fig. 11f) but do not in member 50 (Fig. 11h) at the time of TCG (0600 UTC 3 November). The difference in tropical waves of MRG and MJO is hypothesized to cause the vortex strength differences between GOOD and POOR members, since a stronger MRG wave affects the amplitude of the initial disturbance while a stronger moist MJO signal tends to impact the large-scale environment conditions by not only moistening the lower–midlevel troposphere but also reducing the large-scale VWS by its enhanced tropical westerlies (Figs. 11–12). These differences are believed to be a key factor for a divergence of the ensemble into separate modes.

These results confirm that the uncertainties in the tropical waves can impact the large-scale environment surrounding the precursor and ultimately limit the predictability of tropical cyclone formation and intensity. On average, the ensemble members with stronger equatorial waves eventually lead to stronger TCs, whereas TCs do not form in members with weak or no propagating tropical wave precursors. To further confirm the roles of the MRG and MJO tropical waves, ensemble sensitivity analyses are performed to examine the important factors affecting the genesis of Haiyan in the next section.

6. Ensemble sensitivity analysis on factors affecting the genesis of Haiyan

a. Initial intensity and humidity of the MRG disturbance

Figures 13a–c show the wave decompositions for the GOOD (developer) versus POOR (nondeveloper) groups and their differences. It is apparent that the wave train with alternating cyclonic and anticyclonic TD-type disturbances is stronger in the GOOD group than that

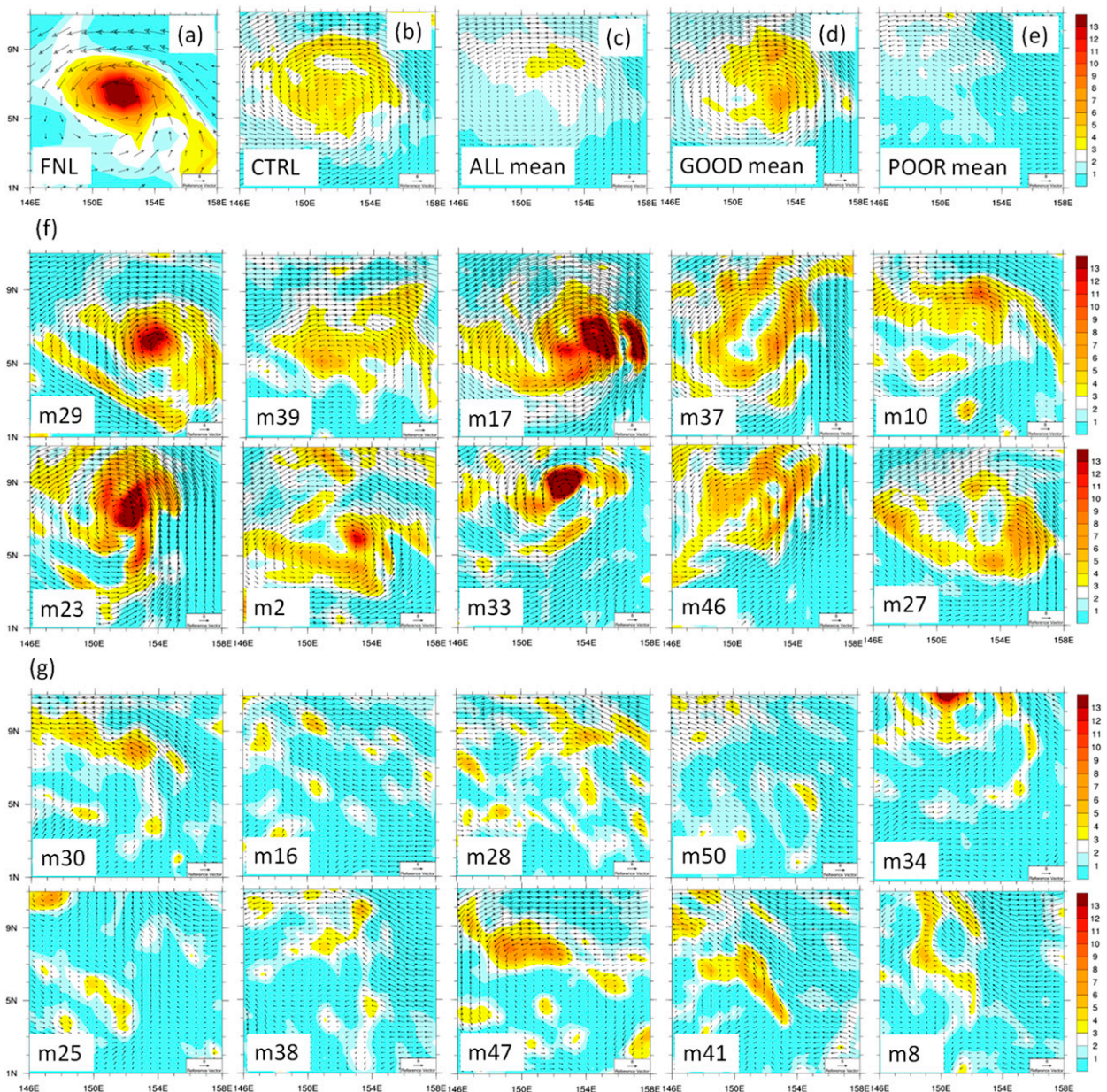


FIG. 9. The 850-hPa wind (vectors; ms^{-1}) and relative vorticity (10^{-5} s^{-1}) (shaded; $1 \times 10^{-5} \text{ s}^{-1}$ intervals) for (a) FNL, (b) CTRL, (c) ALL average, (d) GOOD average, (e) POOR average, and the (f) 10 GOOD members (developers) and (g) 10 POOR members (nondevelopers) at forecast hour 192 (valid at 0000 UTC 4 Nov when Haiyan becomes a tropical storm). In (f) and (g), the member number is indicated in the lower-left corner of each panel. The center of each panel is the observed center of Haiyan from JMA.

seen in the POOR group (Fig. 13c). As stated earlier, this wave train is a combined result of off-equatorial TD-type perturbations, which are transformed from a westward-propagating equatorial MRG wave package with likely contribution of southeastward energy dispersed from preexisting Typhoon Krosa. Taking the pattern at 0000 UTC 1 November, for example, a clear east-southeast-tilted wave train can be discerned in the wake of Krosa in the GOOD composite (Fig. 14a)

but hardly discernible in the POOR composite (Fig. 14b). Both the incipient cyclonic vortex from the MRG wave and the preexisting Typhoon Krosa are stronger in the composite of the developers than those in the nondevelopers.

Previous observational and simulation studies (Li et al. 2003; Li and Fu 2006; Fu et al. 2007) showed that a new TC sometimes formed in the cyclonic vorticity region of a preexisting well-defined wave train because of

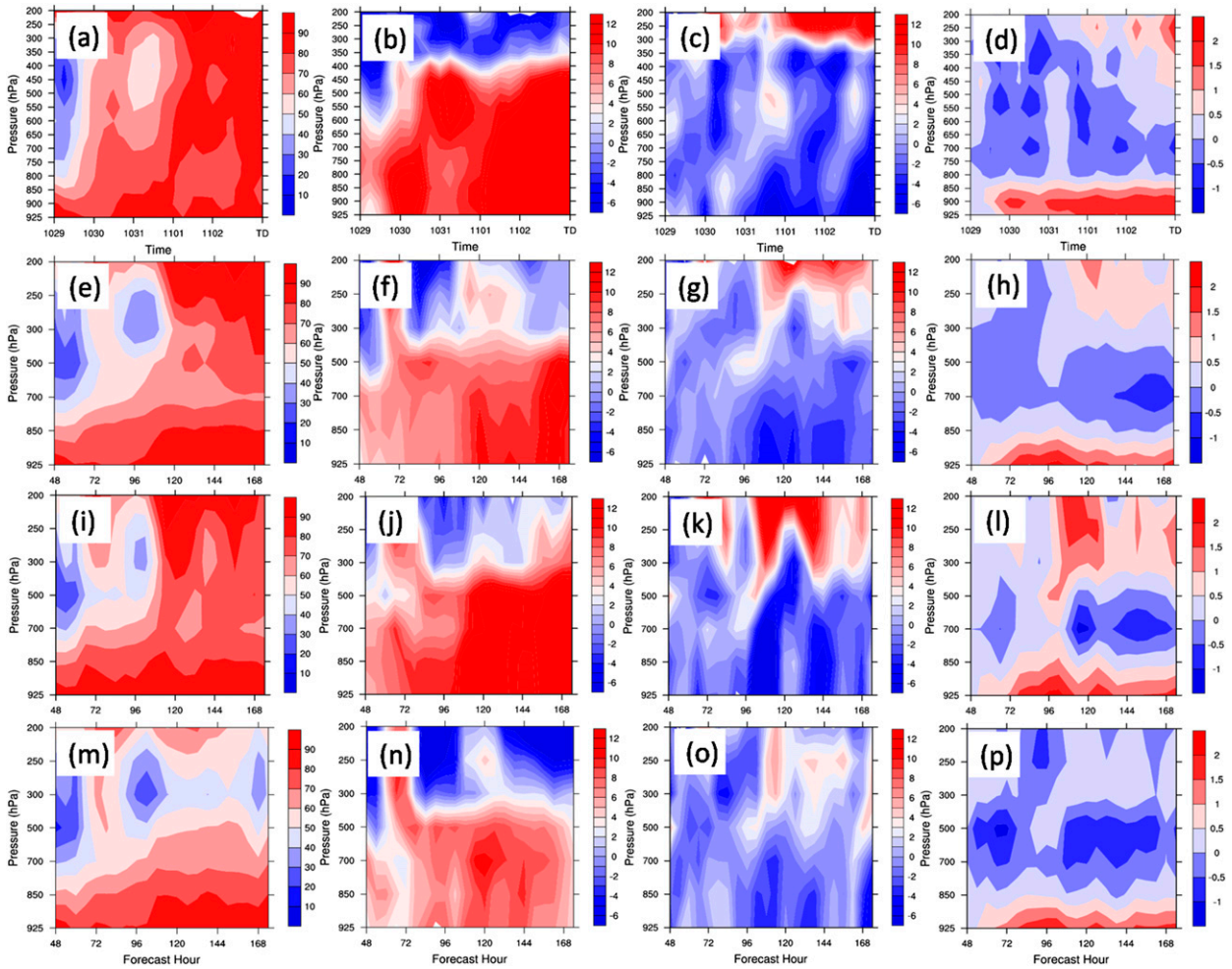


FIG. 10. Comparison of time evolution of the (a),(e),(i),(m) relative humidity (10% intervals), (b),(f),(j),(n) relative vorticity ($1 \times 10^{-5} \text{ s}^{-1}$ intervals), (c),(g),(k),(o) divergence ($1 \times 10^{-5} \text{ s}^{-1}$ intervals), and (d),(h),(l),(p) 200-hPa temperature differences from the 48-h simulated values (valid at 0000 UTC 29 Oct; 0.5°C intervals) averaged over the $10^\circ \times 10^\circ$ storm-relative domain from (a)–(d) FNL, (e)–(h) CTRL, and ensemble forecast members (i)–(l) 29 and (m)–(p) 50.

the TCED. To further examine whether the TC energy dispersion associated with Krosa reaches and influences the precursor of Haiyan, an energy propagation vector \mathbf{E} for preexisting Typhoon Krosa, based on Trenberth (1986) is calculated. Here, $\mathbf{E} = ([-u'u' + v'v']/2, [-u'v'])$, where the square brackets represent time averaging and u' and v' are the zonal and meridional components of 3–6-day bandpass-filtered wind perturbations, respectively. The \mathbf{E} vectors in the bottom row of Fig. 14 are calculated based on a 9-day period from 0000 UTC 28 October to 0000 UTC 6 November 2013. It illustrates that the wave train on the west side of Haiyan’s precursor (top row in Fig. 14) may be indeed corresponding to the southeastward propagation of Rossby wave energy associated with Krosa (bottom row in Fig. 14). The energy emitted from Krosa is stronger in amplitude and broader in area (transmitted to the south of 10°N and

gradually reduced to 140°E) for the developers (Fig. 14c) than that for the nondevelopers (Fig. 14d). The TCED associated with the stronger Krosa in Fig. 14c (mainly confined to about west of 140°E and north of 5°N) is likely to help the development of a new tropical cyclone, TC 30, forming at 0600 UTC 3 November with a distance of 1800 km from Krosa according to the Unisys website (http://weather.unisys.com/hurricane/w_pacific/2013/index.php). The influence of Krosa through TCED is confirmed through our further sensitivity experiments, which find that TC 30 will not be generated if Krosa is significantly weakened in the initial and boundary conditions (not shown). Figure 14c shows that TC 30 also emits Rossby energy along its southeast direction to the incipient Haiyan. However, given Haiyan and TC 30 formed at almost the same time, the contribution of

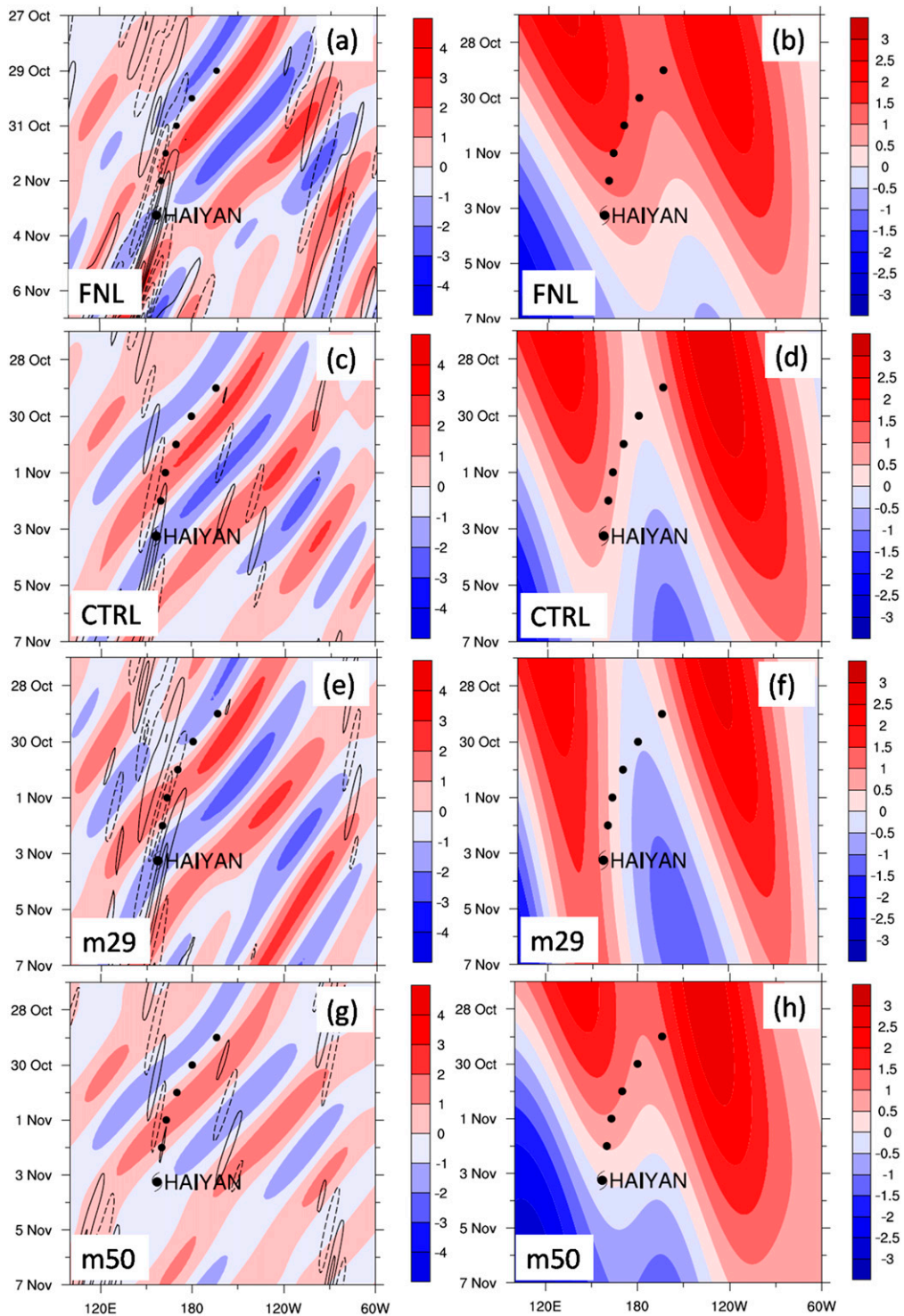


FIG. 11. Wave decomposition from (a),(b) FNL, (c),(d) CTRL, and ensemble forecast members (e),(f) 29 and (g),(h) 50 on scales of MRG (described by 850-hPa meridional wind averaged over a strip of 5°S – 5°N , shaded with 1 m s^{-1} intervals) overlapped with (left) TD (described by 850-hPa meridional wind averaged over a strip of 0° – 15°N , black contoured with 1 m s^{-1} intervals, negative values dashed) and (right) MJO (expressed by 850-hPa zonal wind on equator, shaded with 0.5 m s^{-1} intervals). The typhoon symbol indicates the location of TCG, and the black dots mean the locations of Haiyan's precursor before TCG.

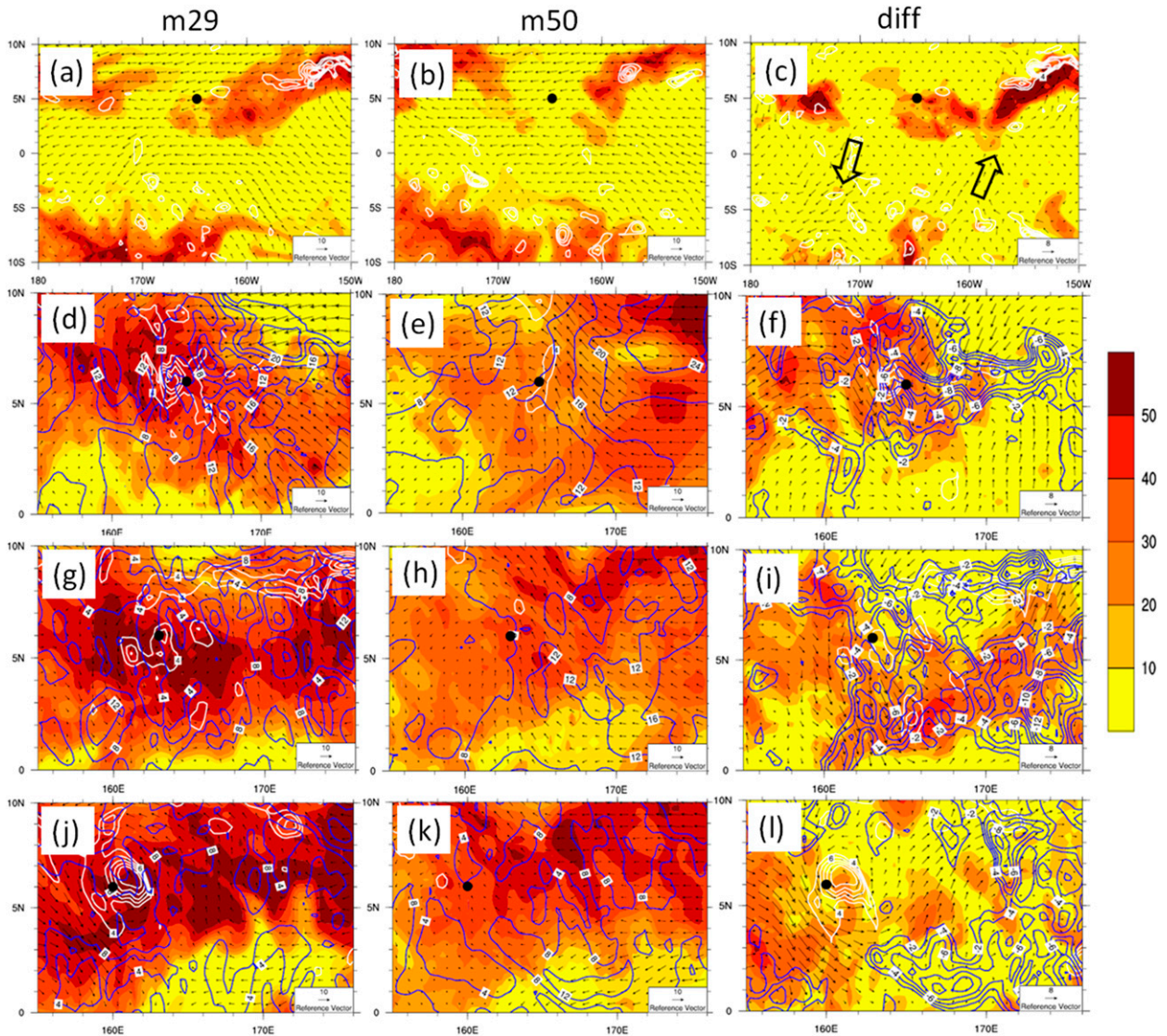


FIG. 12. Large-scale environmental conditions in members (left) 29 and (middle) 50 and (right) difference fields between them (member 29 minus member 50) at (a)–(c) 0600 UTC 29 Oct, (d)–(f) 1200 UTC 31 Oct, (g)–(i) 0600 UTC 1 Nov, and (j)–(l) 0600 UTC 2 Nov for 850-hPa wind (vectors), 500-hPa relative humidity (shaded; 10% intervals), and 850-hPa relative vorticity (white contoured; $2 \times 10^{-6} \text{ s}^{-1}$ intervals starting at $4 \times 10^{-6} \text{ s}^{-1}$). In the bottom three rows, the VWS is also displayed by blue contours (4 m s^{-1} intervals starting at 4 m s^{-1} in m29 and m50, but -2 m s^{-1} intervals starting at -2 m s^{-1} in diff). The black dots represent the estimated vortex centers from FNL.

TCED from TC 30 is likely to be limited to the genesis of Haiyan, which formed at 0600 UTC 3 November with a center at 5.8°N , 157.2°E . More elaborate examination on the potential contribution and impact of TCED from Krosa or TC 30 to the genesis of Haiyan is beyond the scope of the present paper.

To further examine the role of the initial intensity of the tropical wave precursors in Haiyan's genesis, statistical ensemble correlations and sensitivity analysis are calculated following previous studies (e.g., Sippel and Zhang 2008; Munsell et al. 2013). Figure 13b shows the

evolution of the correlation at each height and time between the 1000-km area-averaged relative vorticity and the final intensity in terms of maximum 850-hPa relative vorticity of 51 ensemble members. A positive correlation implies that the stronger the initial vortex (higher relative vorticity) is, the stronger the vortex will finally become. As expected, the relationship between the relative vorticity and final intensity is stronger in the low levels and strongest at the time of TCG. Sixty hours into the forecasting, the correlation below 700 hPa is relatively small (approximately 0.3–0.4) although still

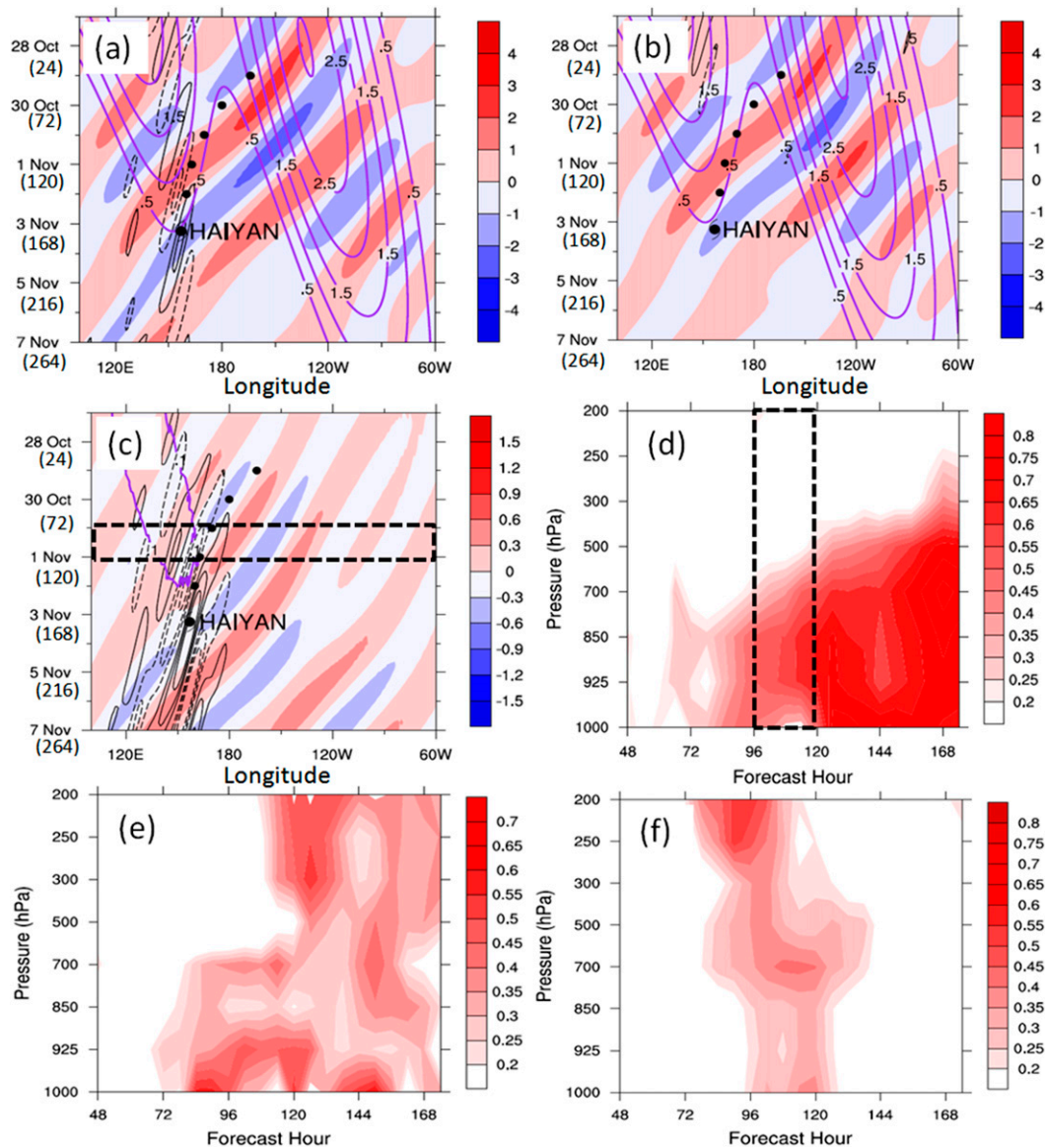


FIG. 13. As in Fig. 11, but for (a) GOOD and (b) POOR groups and (c) their differences. Shading is the MRG scale (0.3 m s^{-1} intervals), black contours mean the TD scale with negative values dashed (0.5 m s^{-1} intervals starting at 0 m s^{-1}), and purple contours represent the MJO scale. The forecast hour corresponding to the date is also shown in parentheses to label the vertical axis. (d) Time–height correlation (every 0.05) between relative vorticity and the final intensity of TCG. (e) Time–height correlation (every 0.05) between relative humidity and the final intensity of TCG. (f) Time–height correlation (every 0.05) between MJO strength (the relative vorticity of the MJO vortex) and the final intensity of TCG. The dashed rectangle indicates the transition period from MRG gyre to TD-type disturbance as shown earlier. A correlation of 0.35, 0.27, and 0.23 is statistically different from 0 with over 99%, 95%, and 90% confidence, respectively.

statistically significant. By forecast hour 78, which is the point in the integration where the characteristics of the ensemble members noticeably begin to separate (Fig. 10), the correlation becomes moderate (approximately 0.4–0.5). After a forecast time of 108 h, which is the time not only that the vigorous deep convection develops but also the MRG gyre transits into a TD-type

disturbance, the correlation becomes very strong (approximately above 0.6) and eventually comes to 0.8 in the midlevels at the time of genesis.

The time–height correlation between relative humidity and final intensity of TCG (Fig. 13e) shows that the low-level relative humidity (below 700 hPa) is positively correlated with the final strength of the vortex in

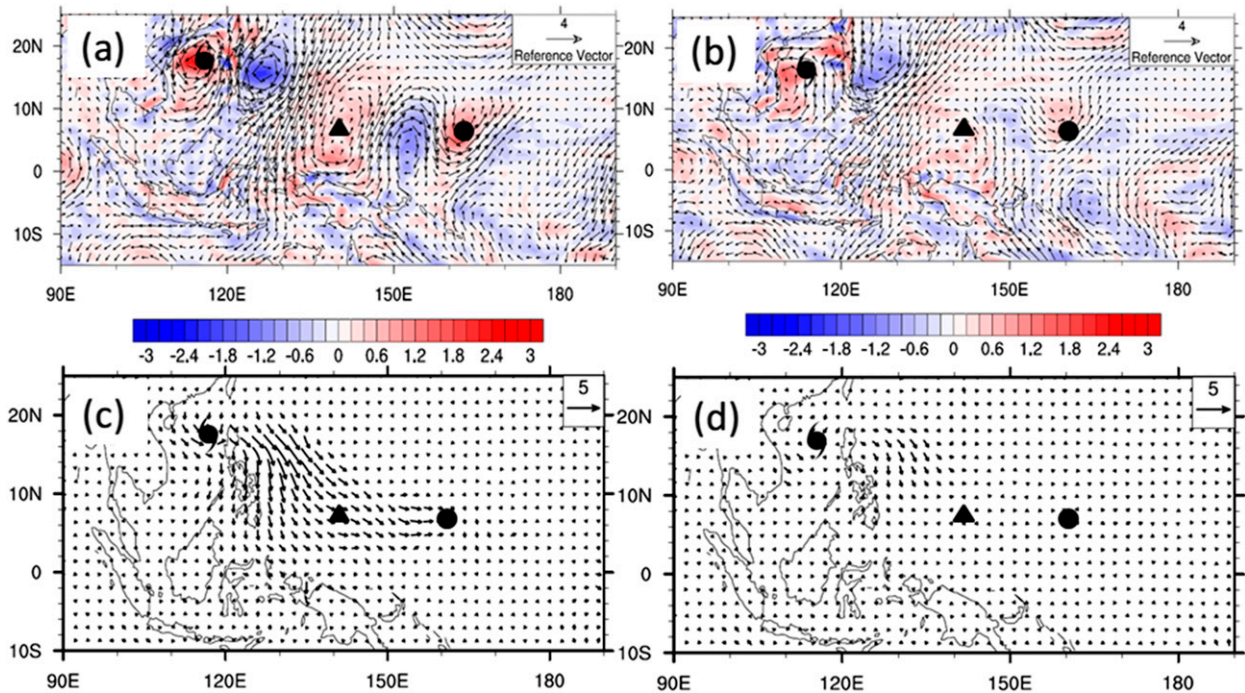


FIG. 14. (a),(b) The 3–6-day synoptic-scale wave train and relative vorticity (shaded with $0.2 \times 10^{-5} \text{ s}^{-1}$ intervals) on 850 hPa at 0000 UTC 1 Nov and (c),(d) horizontal maps of time-averaged \mathbf{E} vectors for (left) GOOD and (right) POOR members; the typhoon symbol, black triangle, and black dot mark the observed position of the preexisting Typhoon Krosa, TC 30, and location of Haiyan's precursor, respectively.

the initial development stage. After the convective bursts (about forecast time of 108 h), the relative humidity in the entire troposphere is positively correlated to the final intensity, accompanying simultaneously the rapid intensification of the cyclonic circulation in the low levels. The analysis of partial correlation between relative humidity and final intensity of TCG while removing the impact of the current intensity shows similar result (not shown). Such a finding agrees with Fang and Zhang (2010, 2011), who pointed out that under the large-scale convergent flow, the induced small-scale positive vorticity anomalies from moist convection could be converged into the storm center and finally lead to the spin up of the system-scale vortex. Our results provide statistical evidence of the importance of the initial intensity and lower-level humidity of the precursor itself in determining the final intensity among the ensemble members. Although they are necessary prerequisites, they however do not completely determine whether a given vortex will intensify or not, especially during the early period of integration (within 72 h) that features relatively low correlations, which is at least partially due to the randomness of the burst of moist convection (e.g., Fang and Zhang 2010; Zhang and Tao 2013).

Figure 13f shows the time–height correlation between MJO strength (the relative vorticity of the MJO vortex)

and the final intensity of TCG. It can be seen from Figs. 13d,f that the MRG wave has a positive correlation with the storm intensity in the initial period before transiting into a TD-type disturbance, whereas the positive correlation of the MJO signal with the storm intensity is significant during the deep convection period (from 96 to 126 h), which also corresponds well with the MRG transition period (0000 UTC 31 October–0600 UTC 1 November), suggesting that the deep convection associated with the MJO facilitates this transition and has a positive impact on the development of Haiyan's precursor. The interaction between the MJO and MRG waves increases uncertainties further and makes genesis of Haiyan less predictable, which can be seen from the sharply increased ensemble spread at forecast hour 126 (valid at 0600 UTC 1 November) in Fig. 8.

b. Westerly and deep convection associated with MJO

Figure 13c also shows that prior to Haiyan's genesis, for developers, the westerlies associated with the MJO are also slightly more apparent in the developer cluster, with positive deviations (purple line) propagating eastward and intersecting with the precursor before TCG. To validate the existence and contribution of the equatorial MJO signal, spatial distributions of partial correlations (shaded) between the 1000-hPa zonal wind and

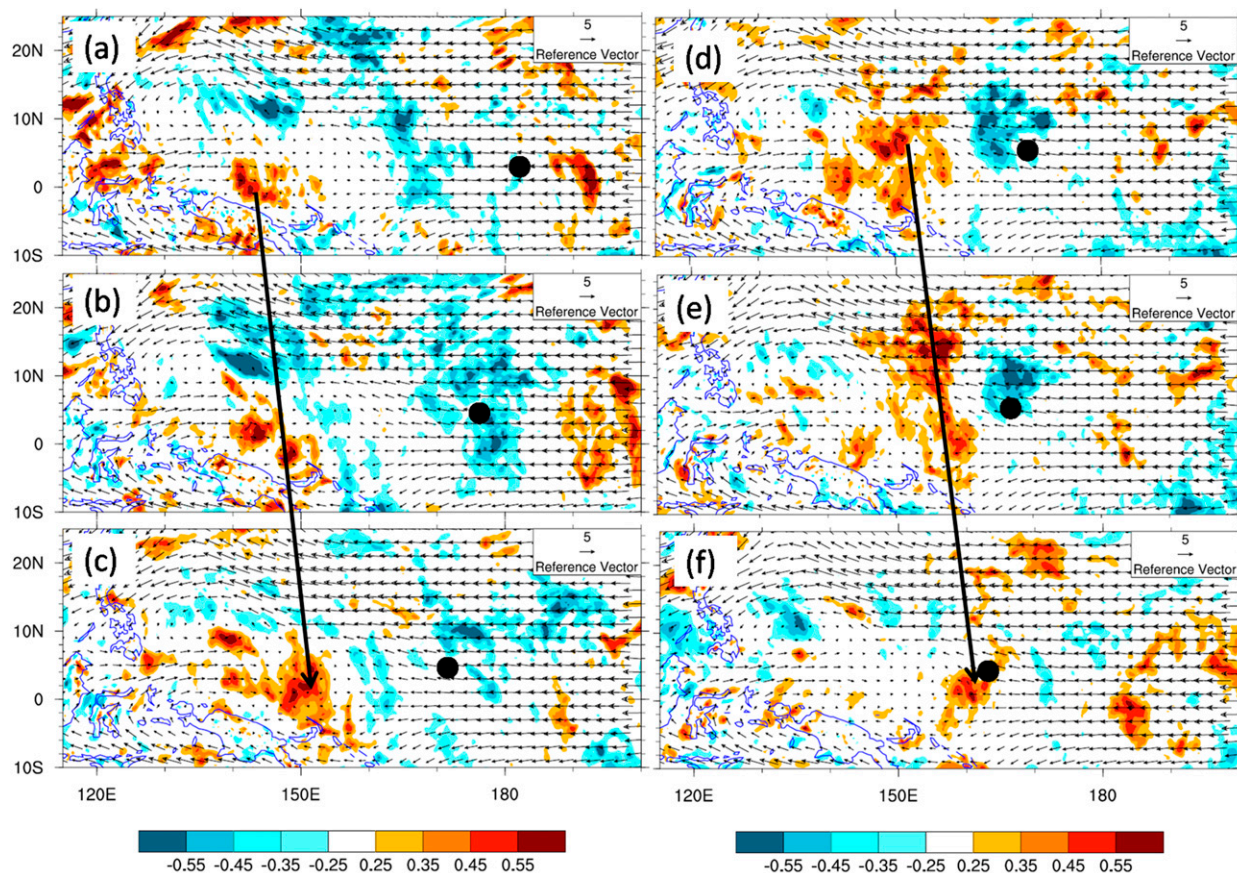


FIG. 15. Partial correlations (every 0.05) between the zonal wind and the final intensity of TCG (while removing the impact that current intensity of the storm has on this relationship) in the 51-member ensemble forecasts and 20–90-day filtered wind (vectors) at 1000 hPa at (a) 1800 UTC 29 Oct, (b) 0600 UTC 30 Oct, (c) 1200 UTC 30 Oct, (d) 0000 UTC 31 Oct, (e) 1200 UTC 31 Oct, and (f) 0600 UTC 1 Nov. The black dots represent the locations of the vortex centers observed from FNL. The long arrows indicate the eastward propagation of the area of positive correlation.

the final intensity of TCG are obtained in Fig. 15. Note that the partial correlation has removed the impact that the current intensity of the storm has on this relationship, following the previous method (e.g., Sippel and Zhang 2008; Munsell et al. 2013), same as below. The MJO-scale filtered wind vectors are also shown to help determine the spatial relationship between the significantly positive area and the MJO circulation. In earlier days (29–30 October) (Figs. 15a–c), an area of significantly positive correlation (red area) propagates slowly eastward near the equator. In later days (31 October–1 November) (Figs. 15d–f), the positive correlation begins to come across the cyclonic precursor that corresponds to the TD-type cyclonic incipient Haiyan transformed from the east MRG wave packet. Since a positive correlation indicates a positive impact on intensification of the TC precursor, this result suggests that the equatorial westerlies associated with the MJO reaching the precursor location from the west may have

also played a positive role in Haiyan’s genesis. The propagation of the MJO can also be confirmed in Fig. 12 where enhanced westerlies lead to decreased vertical wind shear. Correspondingly, both the midlevel moisture and the upper-level temperature (warm anomaly) exhibit similar eastward propagation: the area of positive partial correlations between the 200-hPa temperature and the final genesis intensity of Haiyan (Figs. 16a–c), as well as that between the 500-hPa relative humidity and the final genesis intensity of Haiyan (Figs. 16d–f) also propagates eastward coming across the precursor of Haiyan no later than 1200 UTC 31 October. To confirm the linkage of the upper-level temperature anomaly with the MJO, Figs. 16g–i show the spatial correlations between the 200-hPa-temperature and intensity of the MJO. It can be seen that the positive area (indicating that the upper-level temperature anomaly is positively correlated with MJO strength) comes closer to Haiyan’s precursor before 96 h (0000 UTC 31 October), after

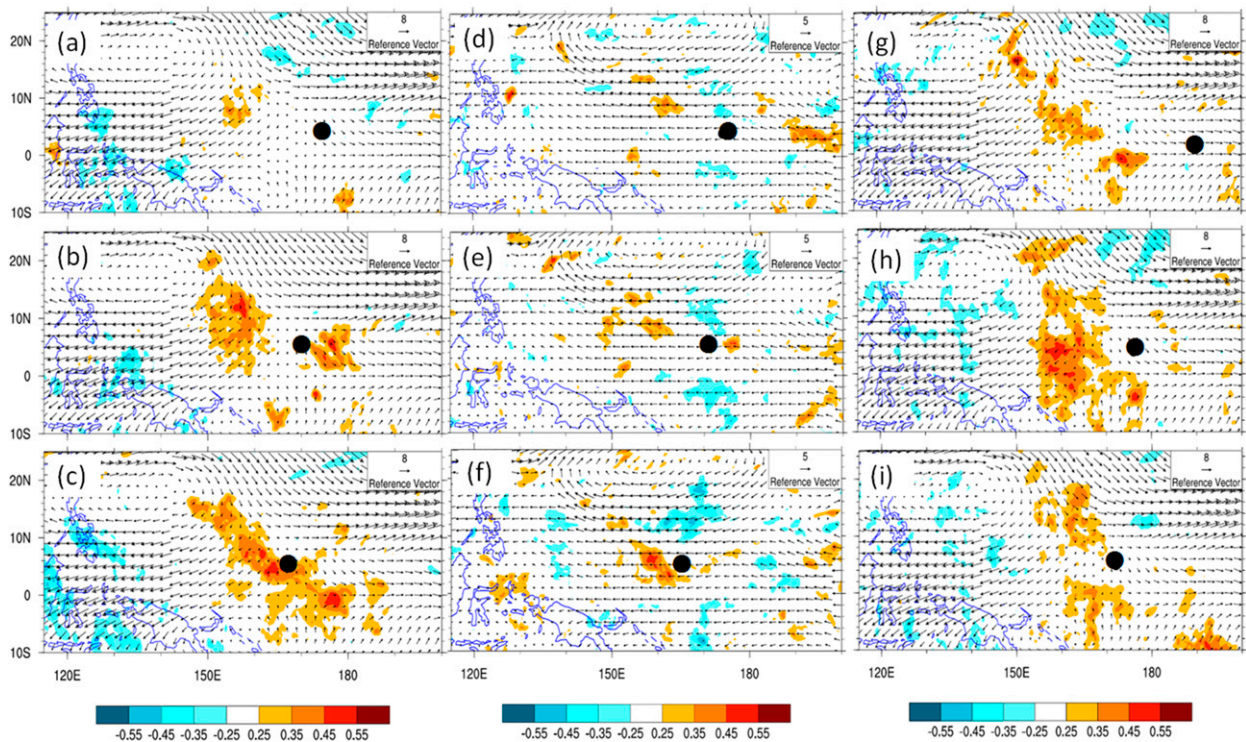


FIG. 16. (left) Partial correlations (every 0.05) between temperature and the final intensity of TCG and 20–90-day filtered wind (vectors) at 200 hPa at (a) 1200 UTC 30 Oct, (b) 0000 UTC 31 Oct, (c) 1200 UTC 31 Oct; (middle) partial correlations (every 0.05) between relative humidity and the final intensity of TCG and 3–6-day filtered wind (vectors) at 500 hPa at (d) 1200 UTC 30 Oct, (e) 0000 UTC 31 Oct, and (f) 1200 UTC 31 Oct; and (right) correlations (every 0.05) between temperature and MJO strength and 20–90-day filtered wind (vectors) at 200 hPa at (g) 0600 UTC 29 Oct, (h) 0600 UTC 30 Oct, and (i) 1800 UTC 30 Oct. The black dots represent the locations of the vortex centers observed from FNL.

which the enhancement of midlevel humidity and upper-level warming associated with the MJO promotes deep moist convection at the precursor location, leading to the rapid intensification of the incipient Haiyan.

The approach of the MJO westerlies, the associated midlevel moistening, and the upper-level warming to the vortex of the precursor around the forecast hour 120 (0000 UTC 1 November) can also be confirmed in Figs. 17a–c. After that time, the intensities of the ensemble members distinctly separate with GOOD members struggling to develop and POOR members dissipating (Fig. 17d) under the favorable large-scale environmental conditions. The interesting finding of the difference in upper-tropospheric warming between developers and nondevelopers before and at TCG (Figs. 10d,h,l,p and 17c) is very consistent with the results emphasized by Cecelski et al. (2014), who indicated that the persistent warmer temperatures at 200 hPa hydrostatically induced falls of the mean sea level pressure and intensification of a meso- β surface low (TD) to Hurricane Julia (2010). Prior to genesis of Haiyan, the increased relative humidity and divergent outflow

precedes the deepening and enhancing of the warming aloft (the bottom two rows in Fig. 10), suggesting the impacts of the deep convection and the associated upper-level divergence on the final formation of TD Haiyan.

From the above analysis, under favorable large-scale environmental conditions, the interaction of the disturbances transformed from the equatorial MRG waves with the eastward-propagating westerlies and convective burst associated with the MJO leads to the final genesis of Haiyan. More work needs to be done to verify how they interact with each other to trigger the burst of mesoscale moist convection and the eventual genesis of Haiyan.

7. Concluding remarks

This study explores the influence of equatorial wave disturbances on the genesis of Super Typhoon Haiyan (2013), which is the most powerful storm ever recorded to strike land (Lander et al. 2014) through spectral, composite, and ensemble sensitivity analysis of various observational datasets in combination with the

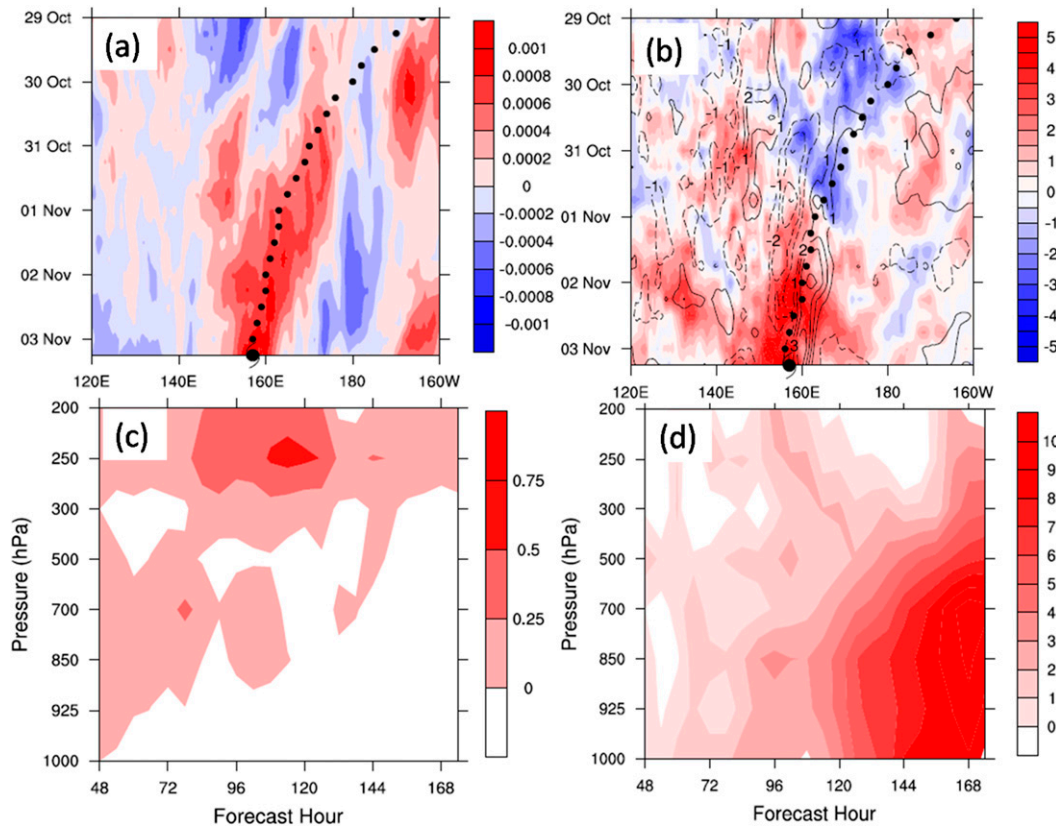


FIG. 17. Longitude–time plot of difference of (a) 500-hPa specific humidity (shaded every 0.2 g kg^{-1}) and (b) 1000-hPa zonal wind (shaded every 0.5 m s^{-1}) and meridional wind (contoured every 1 m s^{-1}) between GOOD and POOR averages. Time–height plot of difference of (c) temperature (shaded every 0.25°C) from the 48-h simulation and (d) area-averaged 850-hPa relative vorticity (every $1 \times 10^{-5} \text{ s}^{-1}$) between GOOD and POOR averages.

51-member ensemble forecasts from ECMWF archived in the TIGGE dataset. It is found that the genesis of Haiyan is a combined result of favorable large-scale environmental conditions and appropriate equatorial wave disturbances, which can be summarized in the schematic (Fig. 18). A TD-type cyclonic disturbance, which transforms from a near-equatorial MRG wave packet when moving northwest, serves as the precursor of Haiyan. Along its westward journey, the large-scale environmental conditions under the influence of the Asian monsoon trough, an extremely warm sea surface ($\text{SST} > 30^\circ\text{C}$), and weak VWS ($< 5 \text{ m s}^{-1}$) become increasingly more favorable for enhancing large-scale cyclonic vorticity and convergence. Moreover, the incipient Haiyan moves into an envelope of an eastward-propagating equatorial MJO wave that has strong low-level convergence, high moisture content, and weak vertical wind shear two days before TCG (around 0000 UTC 1 November). These favorable environmental conditions promote the intensification and aggregation of deep moist convection that facilitates the

development of the cyclonic disturbance from an MRG wave into a tropical depression Haiyan.

Consistent with the observational analyses, the ensemble composite and sensitivity analyses further show that uncertainties in both MRG and MJO waves as well as their interactions can impact the Haiyan's precursor itself and the large-scale environment surrounding it and, therefore, limit the predictability of tropical cyclone formation and intensity. The better-performing members tend to have a stronger initial MRG wave disturbance, which provides a stronger initial seed for the later development of the storm. In the meantime, overall, the better-performing members also tend to be associated with a stronger moist MJO disturbance in the tropical region, which not only promotes deep convection near the precursor location by moistening the midlevel troposphere but also reduces the environmental vertical wind shear by strengthening the tropical westerlies.

Note that, although the large-scale pattern like the monsoon trough or monsoon shear remains basically

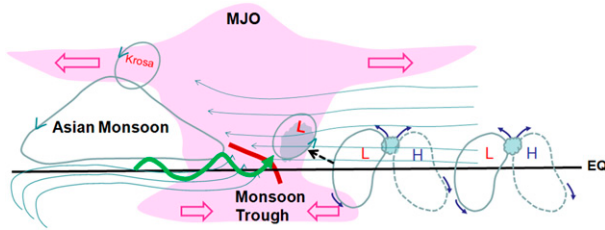


FIG. 18. Schematic of the genesis process of Super Typhoon Haiyan (see text for details). The thick red line indicates the location of the Asian monsoon trough, and the green wave line represents the moist MJO signal in the tropical region.

similar from September to December (e.g., Fig. 2 in Ritchie and Holland 1999) in the WNP, its coupling with the active MJO phase builds a more favorable environment of lower-level convergence and deep moist updraft. Our results also suggest that the predictability of tropical cyclone intensity during the formation and rapid intensification stages may be intrinsically limited in the presence of equatorial waves. Future studies will examine how the uncertainties due to different equatorial waves and their interactions impact this predictability.

It is also worth noting that since correlation does not necessarily imply causality, ongoing and planned experiments with convection permitting regional-scale models will further explore the dynamics and predictability of Haiyan's genesis under the influence of tropical wave disturbances through downscaling the initial and boundary conditions from the ECMWF ensemble.

Acknowledgments. We thank Yonghui Weng for his help on the TIGGE dataset for this work. This study is supported by the project of the National (Key) Basic Research and Development (973) Program of China (2015CB452801), National Natural Science Foundation of China (41575054, 41275057), and State Key Laboratory of Severe Weather, Chinese Academy of Meteorological Sciences (2013LASW-B17). Partial funding support was also provided by the Office of Naval Research Grant N000140910526 and National Science Foundation Grant AGS-130579. The computing is performed at the Texas Advanced Computing Center (TACC).

REFERENCES

- Aiyyer, A. R., and J. Molinari, 2003: Evolution of mixed Rossby-gravity waves in idealized MJO environments. *J. Atmos. Sci.*, **60**, 2837–2855, doi:10.1175/1520-0469(2003)060<2837:EOMRW1>2.0.CO;2.
- Anthes, R. A., 1982: Tropical cyclones: Their evolution, structure and effects. *Meteor. Monogr.*, No. 41, Amer. Meteor. Soc., 208 pp.
- Bougeault, P., and Coauthors, 2010: The THORPEX Interactive Grand Global Ensemble. *Bull. Amer. Meteor. Soc.*, **91**, 1059–1072, doi:10.1175/2010BAMS2853.1.
- Bracken, W. E., and L. F. Bosart, 2000: The role of synoptic-scale flow during tropical cyclogenesis over the North Atlantic Ocean. *Mon. Wea. Rev.*, **128**, 353–376, doi:10.1175/1520-0493(2000)128<0353:TROSSF>2.0.CO;2.
- Briegleb, L. M., and W. M. Frank, 1997: Large-scale influences on tropical cyclogenesis in the western North Pacific. *Mon. Wea. Rev.*, **125**, 1397–1413, doi:10.1175/1520-0493(1997)125<1397:LSIOTC>2.0.CO;2.
- Buizza, R., and T. N. Palmer, 1995: The singular vector structure of the atmospheric global circulation. *J. Atmos. Sci.*, **52**, 1434–1456, doi:10.1175/1520-0469(1995)052<1434:TSSVOT>2.0.CO;2.
- Camargo, S. J., M. C. Wheeler, and A. H. Sobel, 2009: Diagnosis of the MJO modulation of tropical cyclogenesis using an empirical index. *J. Atmos. Sci.*, **66**, 3061–3074, doi:10.1175/2009JAS3101.1.
- Carr, L. E., III, and R. L. Elsberry, 1994: Systematic and integrated approach to tropical cyclone track forecasting. Part I. Approach overview and description of meteorological basis. NPS Tech. Rep. NPS-MR-94-002, 273 pp.
- , and —, 1995: Monsoonal interactions leading to sudden tropical cyclone track changes. *Mon. Wea. Rev.*, **123**, 265–289, doi:10.1175/1520-0493(1995)123<0265:MILTST>2.0.CO;2.
- Cecelski, S. F., D.-L. Zhang, and T. Miyoshi, 2014: Genesis of Hurricane Julia (2010) within an African easterly wave: Developing and nondeveloping members from WRF-LETKF ensemble forecasts. *J. Atmos. Sci.*, **71**, 2763–2781, doi:10.1175/JAS-D-13-0187.1.
- Chang, C. P., J. M. Chen, P. A. Harr, and L. E. Carr, 1996: Northwestward-propagating wave patterns over the tropical western North Pacific during summer. *Mon. Wea. Rev.*, **124**, 2245–2266, doi:10.1175/1520-0493(1996)124<2245:NPWPOT>2.0.CO;2.
- Chang, H.-R., and P. J. Webster, 1990: Energy accumulation and emanation at low latitudes. Part II: Nonlinear response to strong episodic equatorial forcing. *J. Atmos. Sci.*, **47**, 2624–2644, doi:10.1175/1520-0469(1990)047<2624:EAAEAL>2.0.CO;2.
- Chen, G., and C.-Y. Tam, 2012: A new perspective on the excitation of low-tropospheric mixed Rossby-gravity waves in association with energy dispersion. *J. Atmos. Sci.*, **69**, 1397–1403, doi:10.1175/JAS-D-11-0331.1.
- , and C. Chou, 2014: Joint contribution of multiple equatorial waves to tropical cyclogenesis over the western North Pacific. *Mon. Wea. Rev.*, **142**, 79–93, doi:10.1175/MWR-D-13-00207.1.
- Chen, S. S., R. A. Houze Jr., and B. E. Mapes, 1996: Multiscale variability of deep convection in relation to large-scale circulation in TOGA COARE. *J. Atmos. Sci.*, **53**, 1380–1409, doi:10.1175/1520-0469(1996)053<1380:MVODCI>2.0.CO;2.
- Chen, T. C., S. Y. Wang, M. C. Yen, and A. J. Clark, 2008: Are tropical cyclones less effectively formed by easterly waves in the western North Pacific than in the North Atlantic? *Mon. Wea. Rev.*, **136**, 4527–4540, doi:10.1175/2008MWR2149.1.
- Dickinson, M., and J. Molinari, 2002: Mixed Rossby-gravity waves and western Pacific tropical cyclogenesis. Part I: Synoptic evolution. *J. Atmos. Sci.*, **59**, 2183–2196, doi:10.1175/1520-0469(2002)059<2183:MRGWAW>2.0.CO;2.
- Dunkerton, T., and M. Baldwin, 1995: Observation of 3–6-day meridional wind oscillations over the tropical Pacific 1973–1992: Horizontal structure and propagation. *J. Atmos. Sci.*, **52**, 1585–1601, doi:10.1175/1520-0469(1995)052<1585:OODMWO>2.0.CO;2.
- Fang, J., and F. Zhang, 2010: Initial development and genesis of Hurricane Dolly (2008). *J. Atmos. Sci.*, **67**, 655–672, doi:10.1175/2009JAS3115.1.
- , and —, 2011: Evolution of multiscale vortices in the development of Hurricane Dolly (2008). *J. Atmos. Sci.*, **68**, 103–122, doi:10.1175/2010JAS3522.1.

- Frank, W. M., 1982: Large-scale characteristics of tropical cyclones. *Mon. Wea. Rev.*, **110**, 572–586, doi:10.1175/1520-0493(1982)110<0572:LSCOTC>2.0.CO;2.
- , and E. A. Ritchie, 1999: Effects of environmental flow upon tropical cyclone structure. *Mon. Wea. Rev.*, **127**, 2044–2061, doi:10.1175/1520-0493(1999)127<2044:EOEFUT>2.0.CO;2.
- , and —, 2001: Effects of vertical wind shear on the intensity and structure of numerically simulated hurricanes. *Mon. Wea. Rev.*, **129**, 2249–2269, doi:10.1175/1520-0493(2001)129<2249:EOVWSO>2.0.CO;2.
- , and P. E. Roundy, 2006: The role of tropical waves in tropical cyclogenesis. *Mon. Wea. Rev.*, **134**, 2397–2417, doi:10.1175/MWR3204.1.
- , and G. S. Young, 2007: The interannual variability of tropical cyclones. *Mon. Wea. Rev.*, **135**, 3587–3598, doi:10.1175/MWR3435.1.
- Fu, B., T. Li, M. S. Peng, and F. Weng, 2007: Analysis of tropical cyclogenesis in the western North Pacific for 2000 and 2001. *Wea. Forecasting*, **22**, 763–780, doi:10.1175/WAF1013.1.
- , M. S. Peng, T. Li, and D. E. Stevens, 2012: Developing versus nondeveloping disturbances for tropical cyclone formation. Part II: Western North Pacific. *Mon. Wea. Rev.*, **140**, 1067–1080, doi:10.1175/2011MWR3618.1.
- Ge, X., T. Li, and M. S. Peng, 2010: Cyclogenesis simulation of Typhoon Prapiroon (2000) associated with Rossby wave energy dispersion. *Mon. Wea. Rev.*, **138**, 42–54, doi:10.1175/2009MWR3005.1.
- Gray, W. M., 1968: Global view of the origin of tropical disturbances and storms. *Mon. Wea. Rev.*, **96**, 669–700, doi:10.1175/1520-0493(1968)096<0669:GVOTOO>2.0.CO;2.
- , 1998: The formation of tropical cyclones. *Meteor. Atmos. Phys.*, **67**, 37–69, doi:10.1007/BF01277501.
- Hawblitzel, D. P., F. Zhang, Z. Meng, and C. A. Davis, 2007: Probabilistic evaluation of the dynamics and predictability of the mesoscale convective vortex of 10–13 June 2003. *Mon. Wea. Rev.*, **135**, 1544–1563, doi:10.1175/MWR3346.1.
- Heta, Y., 1990: An analysis of tropical wind fields in relation to typhoon formation over the western Pacific. *J. Meteor. Soc. Japan*, **68**, 65–77.
- , 1991: The origin of tropical disturbances in the equatorial Pacific. *J. Meteor. Soc. Japan*, **69**, 337–351.
- Holland, G. J., 1995: Scale interaction in the western Pacific monsoon. *Meteor. Atmos. Phys.*, **56**, 57–79, doi:10.1007/BF01022521.
- Huffman, G. J., and Coauthors, 2007: The TRMM Multisatellite Precipitation Analysis (TMPA): Quasi-global, multiyear, combined-sensor precipitation estimates at fine scales. *J. Hydrometeorol.*, **8**, 38–55, doi:10.1175/JHM560.1.
- Kiladis, G. N., M. C. Wheeler, P. T. Haertel, K. H. Straub, and P. E. Roundy, 2009: Convectively coupled equatorial waves. *Rev. Geophys.*, **47**, RG2003, doi:10.1029/2008RG000266.
- Kuo, H.-C., J.-H. Chen, R. T. Williams, and C.-P. Chang, 2001: Rossby waves in zonally opposing mean flow: Behavior in northwest Pacific summer monsoon. *J. Atmos. Sci.*, **58**, 1035–1050, doi:10.1175/1520-0469(2001)058<1035:RWIZOM>2.0.CO;2.
- Lander, M. A., 1994: Description of a monsoon gyre and its effects on the tropical cyclones in the western North Pacific during August 1991. *Wea. Forecasting*, **9**, 640–654, doi:10.1175/1520-0434(1994)009<0640:DOAMGA>2.0.CO;2.
- , C. Guard, and S. Camargo, 2014: [The tropics] Super Typhoon Haiyan [in “State of the Climate in 2013”]. *Bull. Amer. Meteor. Soc.*, **95** (7), S112–S114.
- Li, T., and B. Fu, 2006: Tropical cyclogenesis associated with Rossby wave energy dispersion of a preexisting typhoon. Part I: Satellite data analyses. *J. Atmos. Sci.*, **63**, 1377–1389, doi:10.1175/JAS3692.1.
- , —, X. Ge, B. Wang, and M. Peng, 2003: Satellite data analysis and numerical simulation of tropical cyclone formation. *Geophys. Res. Lett.*, **30**, 2122–2126, doi:10.1029/2003GL018556.
- Liang, J., L. Wu, and H. Zong, 2014: Idealized numerical simulations of tropical cyclone formation associated with monsoon gyres. *Adv. Atmos. Sci.*, **31**, 305–315, doi:10.1007/s00376-013-2282-1.
- Liebmann, B., and H. H. Hendon, 1990: Synoptic-scale disturbances near the equator. *J. Atmos. Sci.*, **47**, 1463–1479, doi:10.1175/1520-0469(1990)047<1463:SSDNTE>2.0.CO;2.
- , and C. A. Smith, 1996: Description of a complete (interpolated) OLR dataset. *Bull. Amer. Meteor. Soc.*, **77**, 1275–1277.
- , H. H. Hendon, and J. D. Glick, 1994: The relationship between tropical cyclones of the western Pacific and Indian Oceans and the Madden-Julian oscillation. *J. Meteor. Soc. Japan*, **72**, 401–412.
- Luo, Z., 1994: Effect of energy dispersion on the structure and motion of tropical cyclone. *Acta Meteor. Sin.*, **8**, 51–59.
- Maloney, E. D., and M. J. Dickinson, 2003: The intraseasonal oscillation and the energetics of summertime tropical western North Pacific synoptic-scale disturbances. *J. Atmos. Sci.*, **60**, 2153–2168, doi:10.1175/1520-0469(2003)060<2153:TIOATE>2.0.CO;2.
- Matsuno, T., 1966: Quasi-geostrophic motions in the equatorial area. *J. Meteor. Soc. Japan*, **44**, 25–43.
- McDonald, N. R., 1998: The decay of cyclonic eddies by Rossby wave radiation. *J. Fluid Mech.*, **361**, 237–252, doi:10.1017/S0022112098008696.
- Merrill, R. T., 1988: Environmental influences on hurricane intensification. *J. Atmos. Sci.*, **45**, 1678–1687, doi:10.1175/1520-0469(1988)045<1678:EIOHI>2.0.CO;2.
- Molinari, J., K. Lombardo, and D. Vollaro, 2007: Tropical cyclogenesis within an equatorial Rossby wave packet. *J. Atmos. Sci.*, **64**, 1301–1317, doi:10.1175/JAS3902.1.
- Munsell, E., F. Zhang, and D. Stern, 2013: Predictability and dynamics of a nonintensifying tropical storm: Erika (2009). *J. Atmos. Sci.*, **70**, 2505–2524, doi:10.1175/JAS-D-12-0243.1.
- Nakazawa, T., 1986: Intraseasonal variations of OLR in the tropics during the FGGE year. *J. Meteor. Soc. Japan*, **64**, 17–34.
- NDRRMC, 2014: Effects of Typhoon “Yolanda” (Haiyan). SitRep. 107, 62 pp. [Available online at http://www.ndrrmc.gov.ph/attachments/article/1329/Effects_of_Typhoon_YOLANDA_%28HAIYAN%29_SitRep_No_107_14MAR2014.pdf.]
- Nolan, D. S., and M. G. McGauley, 2014: Tropical cyclogenesis in wind shear: Climatological relationships and physical processes. *Cyclones: Formation, Triggers, and Control*, K. Oouchi and H. Fudeyasu, Eds., Nova Science Publishers, 1–35.
- Qian, C., F. Zhang, B. Green, J. Zhang, and X. Zhou, 2013: Probabilistic evaluation of the dynamics and prediction of Supertyphoon Megi (2010). *Wea. Forecasting*, **28**, 1562–1577, doi:10.1175/WAF-D-12-00121.1.
- Reynolds, R. W., N. A. Rayner, T. M. Smith, D. C. Stokes, and W. Wang, 2002: An improved in situ and satellite SST analysis for climate. *J. Climate*, **15**, 1609–1625, doi:10.1175/1520-0442(2002)015<1609:AISAS>2.0.CO;2.
- Ritchie, E. A., and G. J. Holland, 1999: Large-scale patterns associated with tropical cyclogenesis in the western Pacific. *Mon. Wea. Rev.*, **127**, 2027–2043, doi:10.1175/1520-0493(1999)127<2027:LSPAWT>2.0.CO;2.
- Roundy, P. E., and W. M. Frank, 2004: A climatology of waves in the equatorial region. *J. Atmos. Sci.*, **61**, 2105–2132, doi:10.1175/1520-0469(2004)061<2105:ACOWIT>2.0.CO;2.

- Schreck, C. J., and J. Molinari, 2011: Tropical cyclogenesis associated with Kelvin waves and the Madden–Julian oscillation. *Mon. Wea. Rev.*, **139**, 2723–2734, doi:10.1175/MWR-D-10-05060.1.
- Shu, S., J. Ming, and P. Chi, 2012: Large-scale characteristics and probability of rapidly intensifying tropical cyclones in the western North Pacific basin. *Wea. Forecasting*, **27**, 411–423, doi:10.1175/WAF-D-11-00042.1.
- , F. Zhang, J. Ming, and Y. Wang, 2014: Environmental influences on the intensity changes of tropical cyclones over the western North Pacific. *Atmos. Chem. Phys.*, **14**, 6329–6342, doi:10.5194/acp-14-6329-2014.
- Sippel, J. A., and F. Zhang, 2008: A probabilistic analysis of the dynamics and predictability of tropical cyclogenesis. *J. Atmos. Sci.*, **65**, 3440–3459, doi:10.1175/2008JAS2597.1.
- , and —, 2010: Factors affecting the predictability of Hurricane Humberto (2007). *J. Atmos. Sci.*, **67**, 1759–1778, doi:10.1175/2010JAS3172.1.
- Sobel, A. H., and C. S. Bretherton, 1999: Development of synoptic-scale disturbances over the summertime tropical northwest Pacific. *J. Atmos. Sci.*, **56**, 3106–3127, doi:10.1175/1520-0469(1999)056<3106:DOSSDO>2.0.CO;2.
- Takayabu, Y. N., and T. Nitta, 1993: 3–5 day-period disturbances coupled with convection over the tropical Pacific Ocean. *J. Meteor. Soc. Japan*, **71**, 221–246.
- Tao, D., and F. Zhang, 2014: Effect of environmental shear, sea-surface temperature and ambient moisture on the formation and predictability of tropical cyclones: An ensemble-mean perspective. *J. Adv. Model. Earth Syst.*, **6**, 384–404, doi:10.1002/2014MS000314.
- Torn, R. D., and G. J. Hakim, 2008: Ensemble-based sensitivity analysis. *Mon. Wea. Rev.*, **136**, 663–677, doi:10.1175/2007MWR2132.1.
- Tory, K. J., and W. M. Frank, 2010: Tropical cyclone formation. *Global Perspectives on Tropical Cyclones: From Science to Mitigation*, J. C. L. Chan and J. D. Kepert, Eds., World Scientific, 55–91.
- Trenberth, K. E., 1986: An assessment of the impact of transient eddies on the zonal flow during a blocking episode using localized Eliassen–Palm flux diagnostics. *J. Atmos. Sci.*, **43**, 2070–2087, doi:10.1175/1520-0469(1986)043<2070:AAOTIO>2.0.CO;2.
- Tuleya, R. E., and Y. Kurihara, 1981: A numerical study of the effects of environmental flow on tropical storm genesis. *Mon. Wea. Rev.*, **109**, 2487–2506, doi:10.1175/1520-0493(1981)109<2487:ANSOTE>2.0.CO;2.
- Wang, B., and X. Xie, 1996: Low-frequency equatorial waves in vertically sheared zonal flow. Part I: Stable waves. *J. Atmos. Sci.*, **53**, 449–467, doi:10.1175/1520-0469(1996)053<0449:LFEWIV>2.0.CO;2.
- Wang, Z., T. J. Dunkerton, and M. T. Montgomery, 2012: Application of the marsupial paradigm to tropical cyclone formation from northwestward-propagating disturbances. *Mon. Wea. Rev.*, **140**, 66–76, doi:10.1175/2011MWR3604.1.
- Webster, P. J., and H.-R. Chang, 1998: Atmospheric wave propagation in heterogeneous flow: Basic flow constraints on tropical–extratropical interaction and equatorial wave modification. *Dyn. Atmos. Oceans*, **27**, 91–134, doi:10.1016/S0377-0265(97)00003-1.
- Wheeler, M., and G. N. Kiladis, 1999: Convectively coupled equatorial waves: Analysis of clouds and temperature in the wavenumber–frequency domain. *J. Atmos. Sci.*, **56**, 374–399, doi:10.1175/1520-0469(1999)056<0374:CCEWAO>2.0.CO;2.
- Wu, L., H. Zong, and J. Liang, 2013: Observational analysis of tropical cyclone formation associated with monsoon gyres. *J. Atmos. Sci.*, **70**, 1023–1034, doi:10.1175/JAS-D-12-0117.1.
- Yoshida, R., and H. Ishikawa, 2013: Environmental factors contributing to tropical cyclone genesis over the western North Pacific. *Mon. Wea. Rev.*, **141**, 451–467, doi:10.1175/MWR-D-11-00309.1.
- Zhang, F., 2005: Dynamics and structure of mesoscale error covariance of a winter cyclone estimated through short-range ensemble forecasts. *Mon. Wea. Rev.*, **133**, 2876–2893, doi:10.1175/MWR3009.1.
- , and D. Tao, 2013: Effects of vertical wind shear on the predictability of tropical cyclones. *J. Atmos. Sci.*, **70**, 975–983, doi:10.1175/JAS-D-12-0133.1.
- Zhou, X., and B. Wang, 2007: Transition from an eastern Pacific upper-level mixed Rossby gravity wave to a western Pacific tropical cyclone. *Geophys. Res. Lett.*, **34**, L24801, doi:10.1029/2007GL031831.